

**MINISTRY OF EDUCATION AND TRAINING
HANOI UNIVERSITY OF EDUCATION**

DOAN THI THE

**DIFFUSIVE SHOCK
ACCELERATION**

MASTER THESIS IN PHYSICS

HANOI, 2010

**MINISTRY OF EDUCATION AND TRAINING
HANOI UNIVERSITY OF EDUCATION**

DOAN THI THE

**DIFFUSIVE SHOCK
ACCELERATION**

Specialty: Theoretical Physics and Mathematical Physics
Number code: 60.44.01

MASTER THESIS IN PHYSICS

Supervisor: PROF. PIERRE DARRIULAT

HANOI, 2010

ACKNOWLEDGEMENTS

I worked on my master thesis at VATLY, the Vietnam Auger Training Laboratory, in the Institute of Nuclear Science and Technology in Hanoi, under the supervision of Professor Pierre Darriulat. Prof. Pierre Darriulat was always here to guide my work and answer my questions. He is responsible for having involved me in this project. He explained to me the physics content of the project, how to write a simulation code, how to make it work, etc ... He showed me how to approach a research problem and the need to be persistent to accomplish the task. My views on science have changed so much during the time I have been working with him. I am learning from him not only the knowledge, the way to work but the way to live as a good teacher. I owe him my deepest gratitude.

My work would not have been possible without the help of all my dear friends in the VATLY team. I would like to thank them for listening to me, helping me to improve the understanding of my subject, my skills in data analysis and in using the tools that are required. I was always welcome in the group. They shared with me their working experience and helped me whenever I was in trouble. Especially, I am deeply indebted to Dr Pham Thi Tuyet Nhung, who was always ready to help me to overcome the obstacles I might have met and who showed me what to do and gave me so much encouragement.

I thank warmly Professor Dang Van Soa, who gave me encouragement, help and support and gave me confidence in my work and in the successful completion of my thesis.

I gratefully thank the Hanoi University of Education, where I graduated from and studied for my Master degree, in particular my teachers who gave me knowledge and confidence in my ability to keep learning more and more.

I would like to express my gratitude to Dr Vo Van Thuan for his strong and continued support.

I am grateful to the staff of the Institute of Nuclear Science and Technology who gave me a chance to work there and complete my thesis work, as well as financial support from the World Laboratory.

I would like to keep my final warm thanks for my friends and for my family who always encouraged and helped me in my studies and my thesis work.

TABLE OF CONTENTS

INTRODUCTION	2
CHAPTER 1 : COSMIC RAYS	5
1.1 A brief history	5
1.2 The main features	7
1.3 The sources	11
1.3.1 The sun.....	11
1.3.2 Gamma ray astronomy as a tracer of cosmic ray sources	14
1.3.3 Ultra high energy cosmic rays (UHECRs)	16
CHAPTER 2: ACCELERATION IN SHOCKS	18
2.1 Diffusive shock acceleration (DSA) : An introduction	18
2.2 Inter stellar medium (ISM)	20
2.3 Supernovae (SN) and supernovae remnants (SNRs)	21
2.4 Evidence for magnetic field amplification	24
2.5 Large scale shocks	27
CHAPTER 3: DIFFUSIVE SHOCK ACCELERATION	30
3.1 Hydrodynamic shocks	30
3.2 Astrophysical shocks	31
3.3 Acceleration by successive shock traversals	32
3.4 Energy spectrum	34
CHAPTER 4: A SIMPLE SIMULATION	36
4.1 General framework.....	36
4.2 Magnetic field	37
4.3 Uniform magnetic field	38
4.4 Lined-up dipoles.....	42
4.5 Random dipoles.....	43
4.5.1 Generalities	43
4.5.2 H0-M0 resonance.....	48
4.5.3 R-D relation and scaling	50
4.5.4 Energy spectra.....	54
SUMMARY AND CONCLUSIONS	57
APPENDICES	60
Appendix 1: Shock dynamics	60
Appendix 2: Simulation code	63
Appendix 3: Simulation runs	68
REFERENCES	75

INTRODUCTION

The sources of galactic cosmic rays, which form the bulk of those that reach the Earth, have long been unknown. It is only recently, with the advent of X-ray astronomy in space and of gamma-ray astronomy on ground, that it became possible to identify young Super Nova Remnants (SNR) as the most common sources.

Cosmic rays are atomic nuclei, their electric charge implies important distortion of their trajectories in the magnetic field of the disc of the Galaxy and, as a result, it is not possible to tell where they come from. Only at the very highest energies, well above the EeV scale, is it possible to associate cosmic ray showers with optical, X-ray or radio counterparts [1]. Contrary to cosmic rays, gamma rays travel straight in the universe and point back to their sources. They are good at revealing the high energy decay photons coming from neutral pions produced in the interaction of very high energy cosmic rays with interstellar matter (ISM). Gamma ray astronomy detects high energy gamma rays from the Cherenkov light produced by electrons and positrons in the showers induced by their interaction with the upper atmosphere. Such showers are similar to the extensive air showers induced by cosmic rays, but significantly shorter because the radiation length is significantly shorter than the interaction length. Main sources of high energy photons are bremsstrahlung (synchrotron radiation) at low energies and π^0 decays (hadrons) or inverse Compton on the cosmic microwave background (electrons) at high energies. Accurate observations in the TeV range have been made by the High Energy Stereoscopic System (HESS) in Namibia [2] that has shown that many sources have an X-ray counterpart identified as SNR. In 2004, in the wake of earlier less accurate observations [3], HESS made a 33 h live time observation [4] of SNR RX J1713, which, when compared with an X-ray image taken by Rosat in 1996 [5] established that the SNR shell [6] is the source of the gamma ray signal. Later on,

higher resolution X-ray observations [7] revealed the presence of turbulences in the region of the shock with important variations from one year to the next. Many such observations followed, with improved resolution, establishing this way that galactic cosmic rays originate from SNRs.

The identification of SNRs as sources of galactic cosmic rays has suggested an acceleration mechanism, called diffusive shock acceleration (DSA), which is now accepted as the most likely candidate for accelerating cosmic rays [8]. As in a cyclotron, the particle is accelerated locally on traversing the shock (equivalent of the gap between the cyclotron dees) and is guided by magnetic fields on either side in such a way as to come back to the shock (equivalent of the dipole guide field of the cyclotron). However, both the acceleration and guiding processes are very different from the cyclotron case. Guiding is provided by the remnant magnetic field inherited from the parent star, now strongly diluted, and by stochastic collisionless scattering on magnetic turbulences. Indeed, the mean free path is so large in the much diluted ISM that collisions can be neglected and the two colliding media can be seen as carrying nothing else than magnetic fields.

Acceleration is best described in the frame where the particle happens to be and where the magnetic fields are at rest: while bending the particle trajectories, they do not affect its energy, which therefore remains constant. Essential to this argument is the very low density of the ISM in which the particle evolves, making the occurrence of collisions negligible. Eventually, the particle returns to the shock and crosses it. The Lorentz transformation that describes the movement on the other side of the shock always implies acceleration as both media aim at each other with relative velocity β . At each shock traversal, the energy E of the particle increases by ΔE such that $\Delta E/E = \beta$. After n shock traversals it reaches $E_n = E_0(1+\beta)^n$. At some point, however, the particle drifts too far from the shock to have a chance to return to it and escapes.

The aim of the present work is to simulate this acceleration mechanism and to evaluate the role played by magnetic turbulences. The next chapter gives a broad introduction to the physics of cosmic rays and is followed by a chapter that summarizes the main features of acceleration in shocks. *Chapter 3* describes specifically the mechanism of diffusive shock acceleration (DSA) and *Chapter 4* presents the simulation that I performed and the main results. The thesis ends with a short summary and some conclusions.

CHAPTER 1

COSMIC RAYS

1.1 A brief history [9]

At the end of the XIXth century, scientists were puzzled by the spontaneous discharge of their electroscopes which suggested the presence of an ionizing radiation. In 1909, Wulf, on the Eiffel tower, noted that the discharge rate was decreasing with altitude. Between 1911 and 1913 the Austrian physicist Viktor Hess performed balloon measurements reaching up to five kilometres in altitude and established the existence of an “unknown penetrating radiation coming from above and most probably of extraterrestrial origin”. He shared the 1936 Nobel Prize with Carl Anderson.

In the following years, cosmic rays became the subject of intense research, in particular with Millikan (who coined the name in 1925) and Anderson at Pikes peak. In 1927, the dependence on latitude and the east-west asymmetry established unambiguously that cosmic rays were charged particles, not photons. In 1938, Pierre Auger, using counters in coincidence, discovered extensive air showers and understood that they were produced by very high energy (up to $10^{15}eV$) primaries interacting with the earth atmosphere.

In the thirties and forties, when accelerators were not yet dominating the scene, cosmic rays became the laboratory for the study of particle physics. Anderson discovered the positron in 1932 and the muon in 1938. Powell and Occhialini discovered the pion in 1947. Then came strange particles: kaons, hyperons and many others. In the fifties, accelerators took over and cosmic rays got studied for their own sake.



Figure 1: The pioneers (from left to right): Viktor Hess and his balloon, Pierre Auger at the Jungfrauoch, and Anderson with his cloud chamber.

For many years following, major effort was devoted to the study of cosmic rays, trying to understand their origin. Ground detectors, large arrays and fluorescence telescopes, reached very high energies (John Linsley at Volcano Ranch saw the first 10^{20} eV shower in 1962). Space astronomy has been a breakthrough for the study of low energy cosmic rays, in particular solar energetic particles (SEP). A recent example of space measurements in solar astronomy is the NASA's Advanced Composition Explorer (ACE) that was launched from Cape Canaveral in 1997 to the Lagrange point between sun and earth.

In the past 20 years, spectacular progress in astrophysics and long time scales implied in the construction of very high energy accelerators have caused a renaissance of interest in cosmic ray physics under the name of astroparticle physics. In particular TeV gamma ray detectors have been constructed and operated. Their main asset is that they can point to the sources without suffering deflections from magnetic fields. To study cosmic rays, a new generation of ground detectors was born such as the Pierre Auger Observatory, a huge and hybrid detector covering 3000 km^2 where showers are detected from the fluorescence they produce in atmosphere and by their imprint on a ground detector array. Plans to use the whole Earth atmosphere as a radiator observed

from space are being implemented and neutrino astronomy is currently being pioneered.

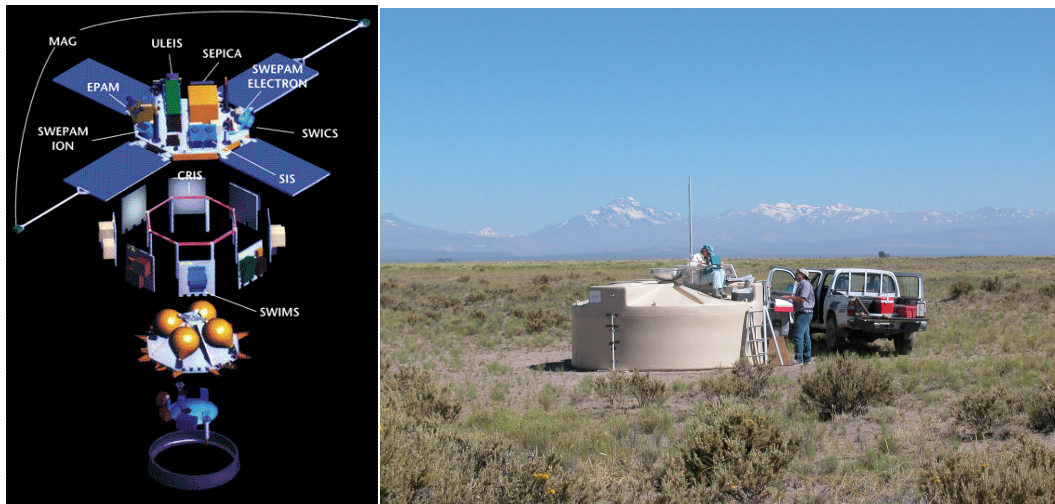


Figure 2: Left: NASA's Advanced Composition Explorer; right: a ground detector of the Auger array.

1.2 The main features

Cosmic rays are ionized nuclei that travel in space up to extremely high energies of the order of $10^{20} eV = 16 \text{ Joules!}$ Cosmic rays having energy in excess of $10^{18} eV$ are referred to as ultra high energy cosmic rays (UHECR). Cosmic rays carry as much energy as the CMB or the visible light or the magnetic fields, namely is $\sim 1 eV/cm^3$. They have a power law energy spectrum spanning 32 decades (12 decades in energy), of the approximate form $E^{-2.7}$.

Whenever they have been measured, cosmic ray abundances are similar to elemental abundances observed in their environment, suggesting that they have been accelerated from interstellar matter. As in any galactic environment, hydrogen and helium dominate, even-even nuclei are naturally favoured and the iron region, which

corresponds to the strongest nuclear binding, is enhanced. The main difference is that the valleys are now filled by spallation reactions on the matter encountered by the cosmic ray during its journey in the interstellar medium, typically $\sim 7 \text{ g cm}^{-2}$.

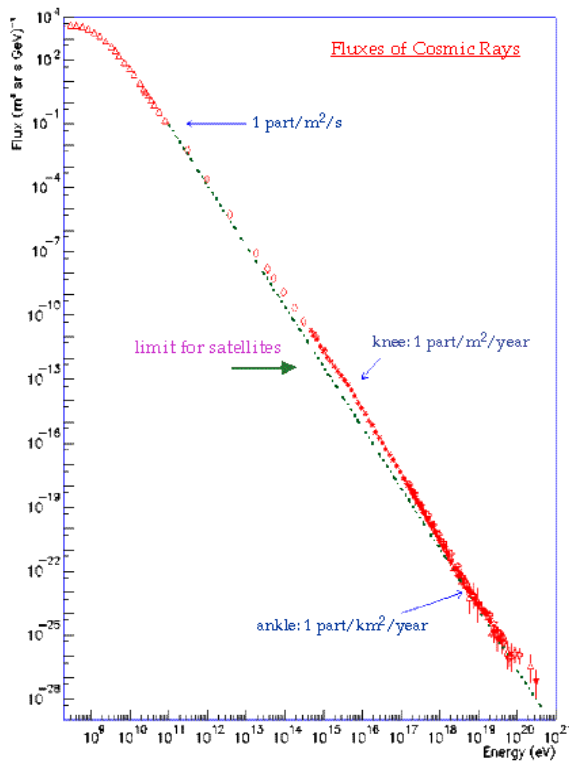


Figure 4: Cosmic ray abundances (full lines) compared with elemental abundances in the Universe (dashed lines). The valleys observed in the latter have been filled up by spallation reactions in the case of cosmic rays.

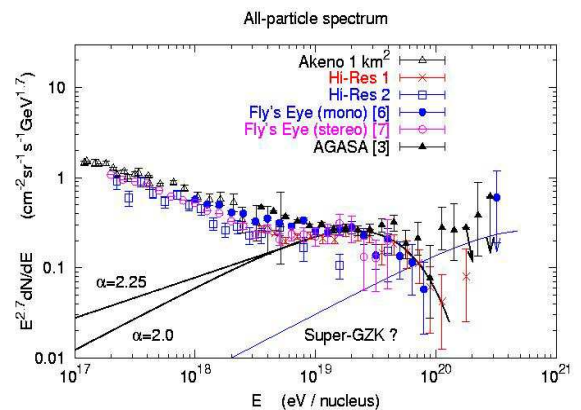
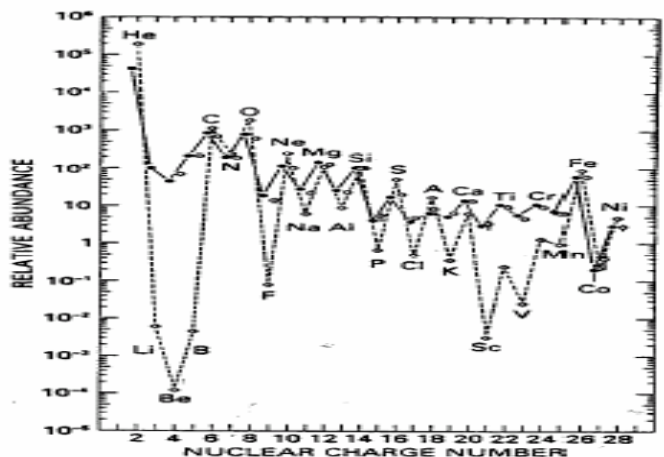


Figure 3: The cosmic ray energy spectrum (left). The same spectrum multiplied by the energy to the power 2.7 is shown in the right panel. The black lines indicate the contribution of extra galactic cosmic rays to the spectrum.



While the very low energy part of the cosmic ray spectrum is of solar origin, most of it does not reach the earth because of its magnetic shield. From the energy spectrum, one evaluates an energy density of the order of $10^{-12} \text{ erg/cm}^3$. Most of it must have a galactic origin because of the magnetic trapping in the Milky Way disk corresponding to a galactic escape time of $\sim 3 \cdot 10^6 \text{ y}$. The cosmic ray power amounts therefore to some $\sim 10^{-26} \text{ erg/cm}^3 \text{ s}$ that can be compared with the power delivered by supernova explosions, $\sim 10^{51} \text{ erg/SN}$ giving, for three SNs explosions per century in the disk, $\sim 10^{-25} \text{ erg/cm}^3 \text{ s}$. Namely cosmic rays carry some $\sim 10\%$ of the power delivered by SN explosions.

It is only in the higher energy part of the spectrum that an extra galactic component can be found. Estimating its energy content requires a low energy extrapolation (*Figure 3, right*) giving an energy density $\rho_{CR} > 2 \cdot 10^{-19} \text{ erg/cm}^3$. One gets from it an estimate of the power needed: $\rho_{CR}/10^{10} \text{ y} \sim 1.3 \cdot 10^{37} \text{ erg/Mpc}^3 \text{ s}$. In comparison, a density of $10^{-7} \text{ AGN/Mpc}^3$ implies $> 10^{44} \text{ erg/s/AGN}$ in order to reach the same energy density, while for 1000 GRB/y one needs $> 3 \cdot 10^{52} \text{ erg/GRB}$. Both active galactic nuclei and gamma ray bursts stand, from the point of view of energy, as possible sources of the cosmic ray extra galactic component.

When a primary cosmic ray enters the Earth atmosphere, it interacts with it and produces a large number of mesons which in turn, interact with the atmosphere, and so on until the primary energy is exhausted in ionization losses. The result is a cascade of interactions producing what is called a shower. UHECR showers contain several billions particles at the maximum of their development and extend transversely on several square kilometres. Their longitudinal profile (*Figure 5 left*) evolves slowly with energy, in proportion to its logarithm, while its energy content, in the form of ionization losses, is proportional to energy. Hence two standard methods to detect extensive air showers: detecting the fluorescence light produced by the shower in the

atmosphere using adequate telescopes or detecting the imprint of the shower on ground by using a large array of detectors.

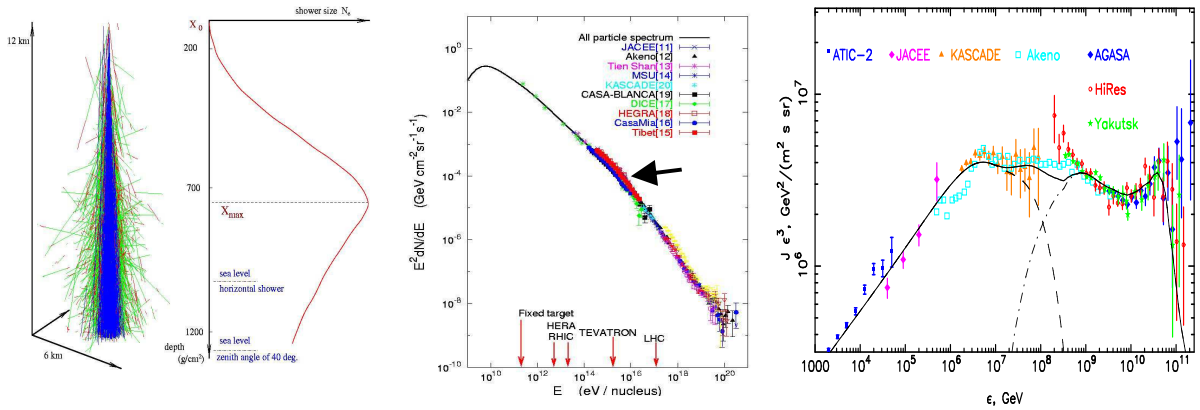


Figure 5: Left: shower development; centre: knee and ankle; right: disentangling different components.

In both cases, the direction of the shower is obtained by measuring the timing of the signals detected and its energy by measuring their intensities. As the former method measures the longitudinal profile of the shower and the latter its transverse profile, they suffer very different systematic uncertainties and are highly complementary. The Pierre Auger Observatory, with 1600 ground detectors over 3000 km^2 and 24 fluorescence telescopes uses both methods simultaneously.

The differential spectral index of the energy spectrum changes at $\sim 10^{15} \text{ eV}$ from 2.7 to 3.0 , this is referred to as the knee. It changes again back to 3 at the upper end of the spectrum, this is referred to as the ankle (Figure 5, centre). These deviations from a pure power spectrum are related to the origin of the cosmic rays in the energy intervals of relevance (galactic or extra-galactic) and are not understood in details; yet, sensible scenarios can be produced which reproduce well the data (Figure 5, right). Of relevance to such scenarios are the interactions of cosmic rays with the cosmic microwave background (CMB), producing either electron-positron pairs or new mesons.

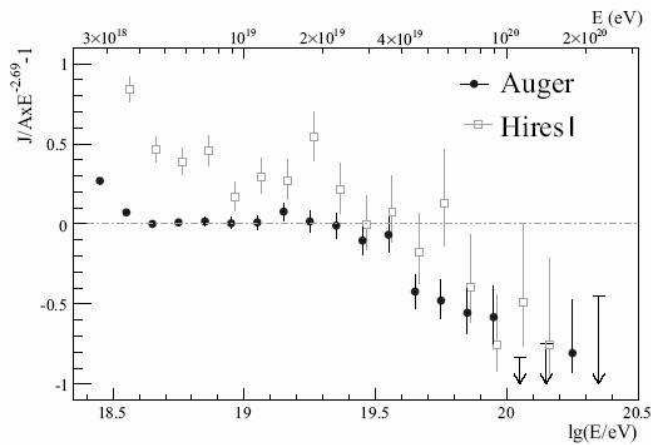


Figure 6: Evidence for the GZK cut-off.

With a typical interaction length in the few 10 Mpc scale, cosmic rays coming from larger distances cannot make it to the Earth without interacting, and therefore lose energy: their flux is significantly damped and only nearby ($< 100 \text{ Mpc}$) sources can contribute to the UHECR spectrum,

1.3 The sources

1.3.1 The sun

Particles coming from the sun (Figure 7) reach at most 100 MeV and are mostly associated with solar activity and flares (magnetic field lines recombination and field inversion with an 11 yr cycle). They have too low a kinetic energy to reach the earth that is protected by the geomagnetic field acting as a shield against cosmic rays having energies smaller than a few GeV ($\sim 4 \text{ GeV}$ in Europe and the U.S., $\sim 14 \text{ GeV}$ in Japan, $\sim 17 \text{ GeV}$ in Vietnam).

Of these, the pion photoproduction threshold is of particular importance and causes the so-called Greisen-Zatsepin-Kuzmin (GZK) cut-off at the end of the spectrum. Until recently, the existence of this cut-off was controversial but the Pierre Auger Observatory has settled the issue (Figure 6) and given clear

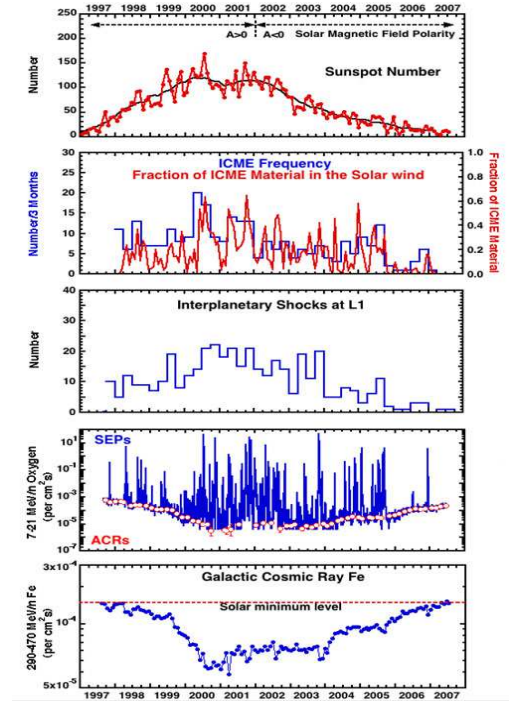
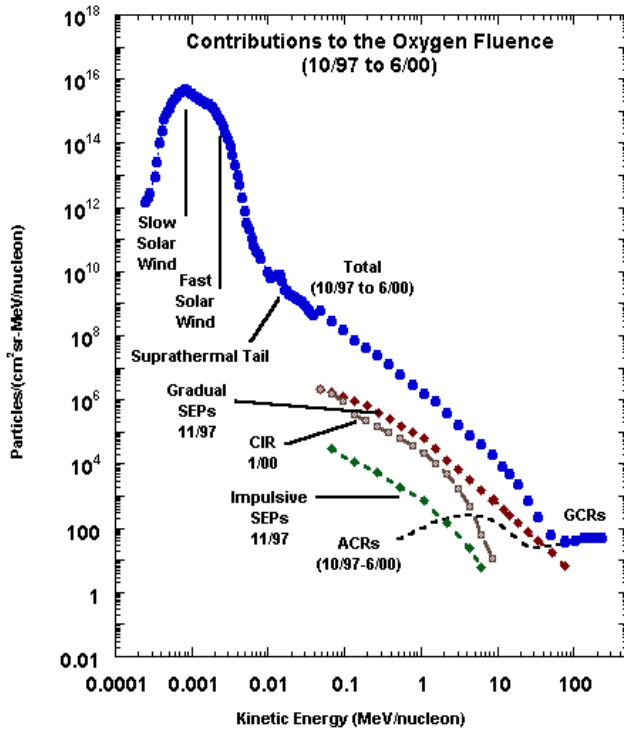


Figure 7: Energy distribution of Sun energetic particles (left) and time structure of solar activity (right).

Coronal Mass Ejections (CME) and interplanetary shocks (most are caused by CME) are similarly correlated with solar activity. On the contrary, galactic cosmic rays are anticorrelated as solar activity increases the magnetic field which acts as a shield.

When observing the Sun with appropriate filters, the most immediately visible features are usually its sunspots, which are well-defined surface areas that appear darker than their surroundings because of lower temperatures. Sunspots are regions of intense magnetic activity where convection is inhibited by strong magnetic fields, reducing energy transport from the hot interior to the surface. The magnetic field gives rise to strong heating in the corona, forming active regions that are the source of

intense solar flares and coronal mass ejections. The largest sunspots can be tens of thousands of kilometres across. The number of sunspots visible on the Sun is not constant, but varies over the *11-year* solar cycle. Sunspots usually exist as pairs with opposite magnetic polarity. The Sun is presently near the end of an unusual sunspot minimum, lasting far longer and with a higher percentage of spotless days than normal [10]; however, recently, it has shown signs of waking up (*Figure 8*).

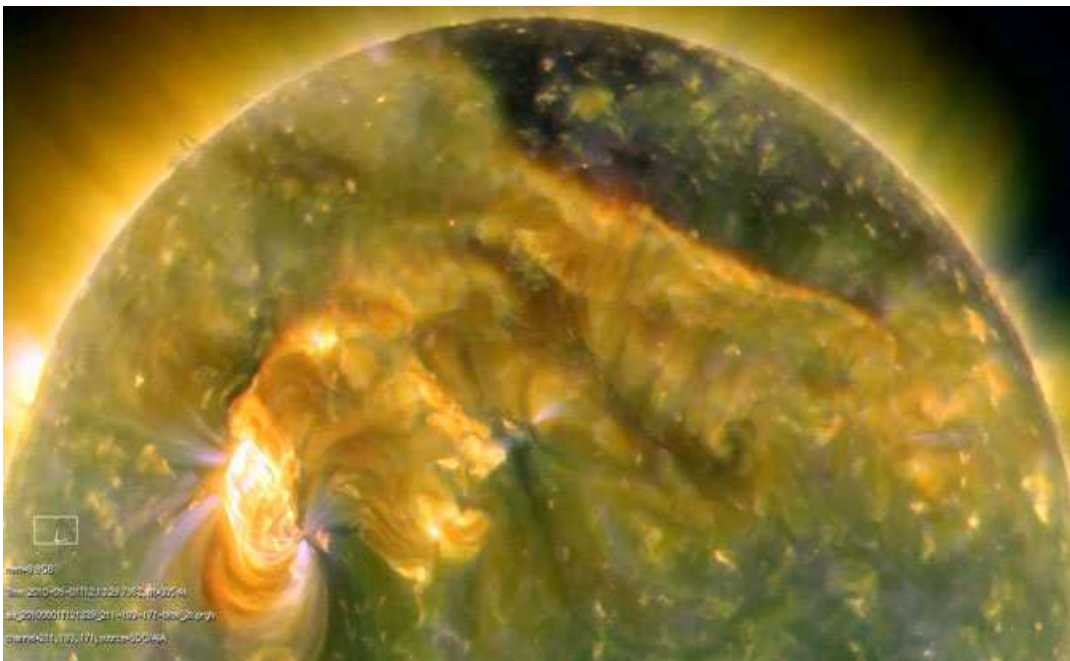


Figure 8: (quoted from Reference 11). “On August 1st, 2010, almost the entire Earth-facing side of the Sun erupted in a tumult of activity. There was a C3-class solar flare, multiple filaments of magnetism lifting off the solar surface, large scale shaking of the solar corona, radio bursts, a coronal mass ejection, and more. This extreme UV snapshot from the Solar Dynamics Observatory (SDO) shows the Sun northern hemisphere in mid eruption. Different colours in the image represent different gas temperatures ranging from to ~1 to ~2 million Kelvin.”

Being close to the earth, the sun is a privileged laboratory for the study of the behaviour of a hot plasma and of the strange dynamic properties that it displays, in

particular the resonant oscillations that it maintains in the form of Alfvén waves. Plasma physics governs most of the phenomena of relevance to the physics of the heliosphere, including solar wind, ejections, shock waves and magnetic field configurations. Such phenomena are in turn of utmost relevance to the understanding of diffusive shock acceleration.

1.3.2 Gamma ray astronomy as a tracer of cosmic ray sources

Contrary to cosmic rays, gamma rays travel straight in the universe and point back to their sources. They are good at detecting the high-energy decay photons coming from neutral pions produced in the interaction of very high-energy cosmic rays with interstellar matter. Gamma ray astronomy detects high energy gamma rays from the Cherenkov light they produce when entering the upper atmosphere and producing electron-photon showers similar to the extensive air showers produced by cosmic rays but significantly shorter (because the radiation length is significantly shorter than the interaction length). It has shown that many sources have an X ray counterpart identified as a Supernova remnant (SNR). It has established this way that most galactic cosmic rays originate from SNRs.

Main sources of high energy photons are bremsstrahlung (synchrotron radiation) at low energies and π^0 decays (hadrons) or inverse Compton on CMB (electrons) at high energies. HESS TeV observations (*Figure 9*) have revealed numerous shell-type SNRs (*Figure 10*) and established that the shell is the source of the gamma ray signal (*Figure 11*).



Figure 9: The High Energy Stereoscopic System (HESS, Namibia) includes four telescopes at the corners of a $120 \times 120 \text{ m}^2$ square, operating above 100 GeV. Its field of view is 5° and its resolution a few arc minutes. To take a picture of the Crab takes only 30 seconds.

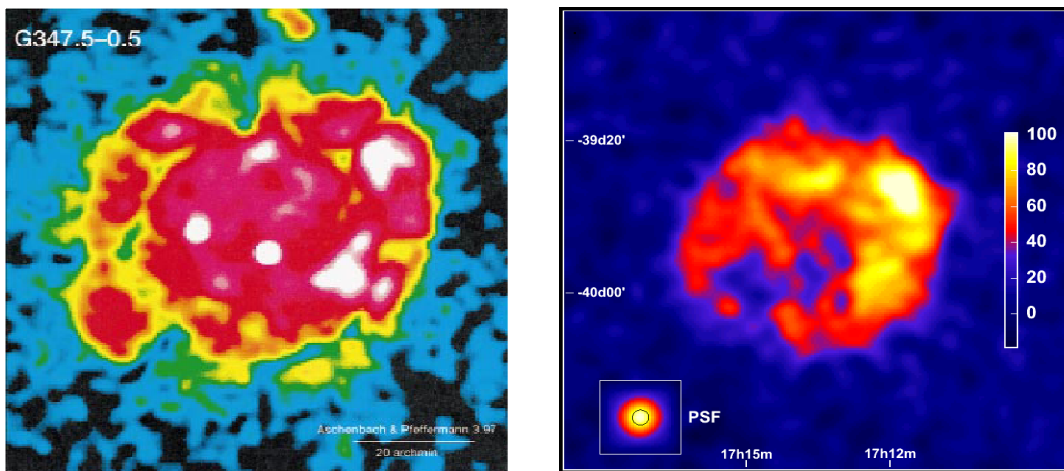


Figure 10: SNR RX J1713 was seen in X ray in 1996 by ROSAT (left). The X ray spectrum revealed mostly non-thermal X-rays and the diameter was measured $\sim 1 \text{ kpc}$. The HESS picture (right) was taken in 2004 and took 33 h live time with all four telescopes. The SNR shell is resolved.

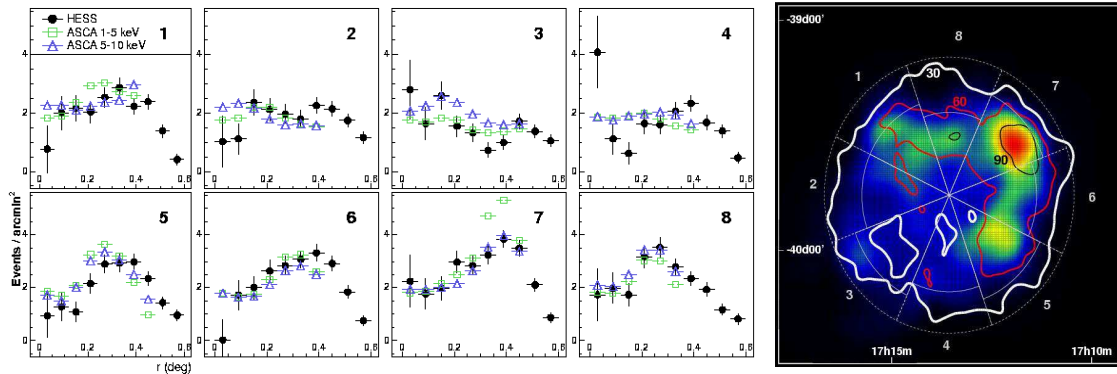


Figure 11: Comparison of radial intensity profiles measured in X and γ rays in separate octants of SNR RX J1713. The overall correlation coefficient between the two radial distributions is 80%.

1.3.3 Ultra High Energy Cosmic Rays (UHECR)

Until recently, it had not been possible to do cosmic ray astronomy because the image of the sources was blurred by magnetic fields. The large UHECR statistics accessible to the Pierre Auger Observatory is now making it possible and reveals a clear correlation with galactic counterparts. Of relevance to this study is the fact that the nearby universe (100

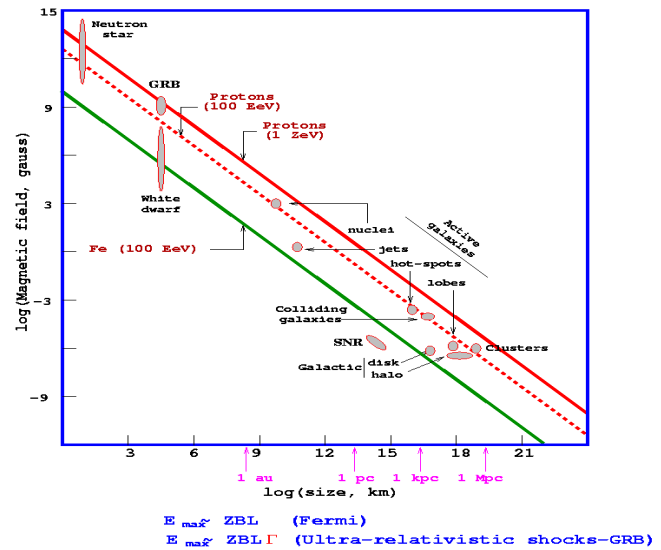


Figure 12: Hillas plot; the upper lines are for protons of 100 and 1000 EeV.

Mpc radius), in which detected UHECRs are confined by the GZK cut-off, is highly inhomogeneous. Selecting UHECR observed at the Pierre Auger Observatory with energy in excess of $6 \cdot 10^{19}$ eV (to prevent significant magnetic bending) and comparing

the direction in the sky where they come from with a catalogue of nearby ($<75 \text{ Mpc}$) galaxies, reveals a significant correlation. There is an even better correlation with nearby AGNs (of which, however, we do not have complete catalogues). The correlation disappears when including lower energy cosmic rays (pointing accuracy) or farther away galaxies (GZK) [12].

This result establishes the ability to point to sources in the sky, typically within 1° , which was not a priori obvious because of uncertainties in magnetic fields met by UHECR during their journey to the Earth (typically $3\mu\text{G}$ in the disk mean $6 \cdot 10^{17} \text{ eV}$). A new page of astronomy has been opened as, until now, only photons could be used. It remains to be understood why such and such a galaxy, AGN or else, is a source while such and such another is not.

Neutrino astronomy is currently actively pioneered and is next to come.

Note that not many celestial objects have large enough *magnetic field* \times *volume* to be candidate sites for UHECR acceleration: as shown in *Figure 12*, the so-called Hillas plot, apart from magnetars, which would suffer of excessive synchrotron losses, the only possible candidates are gamma ray bursts (GRB) or active galaxies, already mentioned when commenting on the amount of energy, which they release.

CHAPTER 2

ACCELERATION IN SHOCKS

2.1 Diffusive shock acceleration: an introduction

The identification of SNRs as sources of galactic cosmic rays has suggested an acceleration mechanism, called diffusive shock acceleration, which is now accepted as the most likely candidate for accelerating cosmic rays. As in a cyclotron (*Figure 13*) the particle is accelerated locally on traversing the shock (equivalent of the gap between the dees) and is guided

by magnetic fields on either side in such a way as to come back to the shock (equivalent of the dipole guide field). However both the acceleration and guiding processes are very different from the cyclotron case. Guiding is provided by the remnant of the parent star

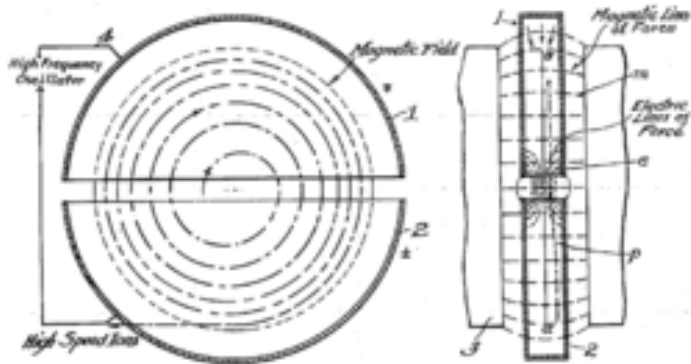


Figure 13: Schematic of a cyclotron.

magnetic field that has not been trapped in the neutron star, now strongly diluted, and by stochastic collisionless scattering on magnetic turbulences. Indeed, the mean free path is so large in the much diluted interstellar medium (ISM) that collisions can be neglected and the two colliding media can be seen as carrying only magnetic fields.

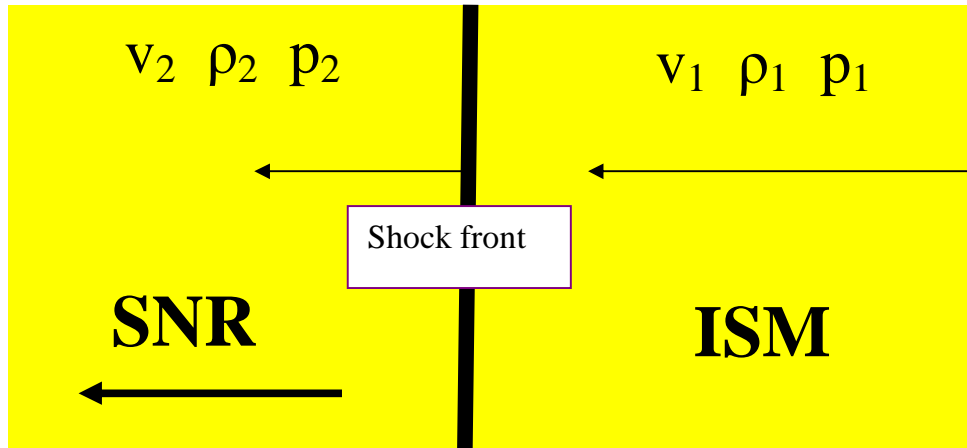


Figure 14: Schematic view of the shock dynamic in the reference frame where the shock is at rest. The flow is from the ISM (upstream) toward the SNR (downstream).

When seen in the frame where the shock is at rest (called the shock frame), both upstream and downstream media move toward the SNR with large velocities (Figure 14). For this reason one calls upstream the ISM side, although it is the downstream side in the ISM rest frame. Similarly, the upstream side in the ISM rest frame, namely the SNR side, is called the downstream side. Indices 1 and 2 refer to the upstream and downstream sides respectively. In the shock frame, the flow velocity is larger upstream than downstream, $v_1 > v_2$. Conversely, the densities obey the relation $\rho_1 < \rho_2$.

However, seen from one medium (any of the upstream or downstream media), the other is moving toward it with a velocity β that is the same in both cases. A cosmic ray traversing the shock does not notice its presence but finds itself in a medium with respect to which it is now moving faster: it has therefore gained energy, whatever direction it is aiming at. The new medium in which it now is, which has to be seen essentially as a moving magnetic field configuration, will ultimately bend it back to the shock front which it will again traverse, again gaining energy. As magnetic forces do not work, (they are normal to the momentum) bending in a magnetic field does not

cause any loss of energy (except by synchrotron radiation in the case of very light and fast particles such as electrons). Multiple traversal of the shock front will therefore take place, each time giving the cosmic ray a small acceleration. Precisely, the energy $E+\Delta E$ of the cosmic ray (mass M) after having traversed the shock is given as a function of its energy E before having traversed the shock as $E+\Delta E = \gamma\beta E + \gamma p$ with $\gamma^2 = \gamma^2\beta^2 + 1$ and $E^2 = p^2 + M^2$. As for $\beta \ll 1$ we have $\gamma \sim 1$ and $p = E$, we get for relativistic cosmic rays: $\Delta E = \beta E + O(\beta^2)$.

$\Delta E/E = \beta$ implies $E_n = E_0(1+\beta)^n$ after n shock traversals. One speaks of first order Fermi acceleration and the acceleration mechanism associated with multiple successive traversals is referred to as diffusive shock acceleration (DSA).

2.2 Inter Stellar Medium (ISM)

Not static, but continuously recycled through star collapses, the ISM is made of three basic constituents: matter, magnetic fields and cosmic rays. In the Milky Way, it amounts to 10-15% of the disk mass, half of it in clouds occupying 1-2% of the ISM volume, mostly very cold dark molecular, peaking at $R = 5 \pm 2$ kpc, and cold diffuse atomic, extending from 0 up to 20 kpc. Elemental abundances are close to those in the solar system, 91% H. About 0.5-1% in mass is in the form of dust. OB associations and SNs affect ISM through winds, radiation, heating, ionization and explosions. In the energy range considered here actual collisions between cosmic rays, and ISM can be ignored and the bending of their trajectories is the result of the presence of magnetic fields.

Typical ISM magnetic fields are at the μG scale as revealed by measurements of star light polarization (due to spinning dust grains aligned on B). Local field is parallel to the galactic plane and tangential Zeeman splitting (on the 21cm HI line) shows an ISM field in the few μG region with little dependence on density. Faraday rotation of

the plane of linear polarization of pulsars gives the B component along the line of sight in the warm ionized medium: uniform and random components at the μG scale. Synchrotron radiation of all sky radio continuum due to cosmic rays suggests again a few μG scale.

<i>Component</i>	<i>T(K)</i>	<i>Observation tool</i>	<i>N(cm⁻³)</i>
<i>Molecular</i>	<i>10-20</i>	<i>2.6mm CO</i>	<i>10²-10⁶</i>
<i>Cold atomic</i>	<i>50-100</i>	<i>21cm H_I</i>	<i>20-50</i>
<i>Warm atomic</i>	<i>6 000-10 000</i>	<i>21cm H_I</i>	<i>0.2-0.5</i>
<i>Warm ionized</i>	<i>~8 000</i>	<i>Dispersion pulsar signals</i>	<i>0.2-0.5</i>
<i>Hot ionized</i>	<i>~10⁶</i>	<i>UV abs lines X soft emission</i>	<i>A few 10⁻³</i>

2.3 Supernovae and SNRs

There exist two main types of supernovae, Ia and II (*Figure 15*).

Type Ia: a white dwarf, member of a binary, accreting from its companion until reaching Chandrasekhar mass of 1.4 solar masses. The core is fully burned, the SNR shell is empty.

Type II: a massive star collapsing into a neutron star that remains in the centre, possibly detected as a pulsar (as in the Crab) the wind of which gives energy to the remnant (one speaks of a plerion).

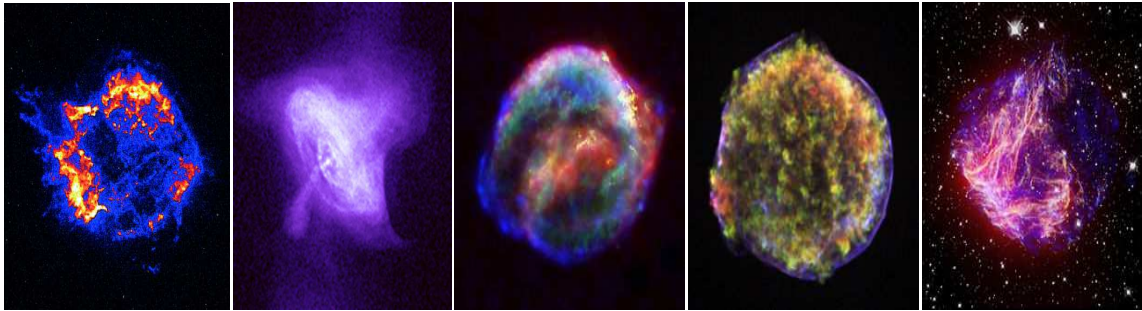


Figure 15: Very high resolution X ray images can presently be obtained of SNRs. From left to right: Cassiopeia A, the Crab, Kepler (SN 1604), Tycho (SN 1572) and N49.

X ray spectra are dominated by thermal emission at $\sim 1\text{keV}$. Optically thin plasma means strong atomic lines (C to Fe), stronger in young SNRs (enriched ejecta). Type Ia progenitors yield more Si/S/Ar/Fe than Type II. In Type Ia, there is complete burning of C-O and the white dwarf produces mostly Fe-peak nuclei (Ni, Fe, Co) with some intermediate masses (O, Si, S, Ar...) giving a very low O/Fe ratio. In type II, the explosive nucleosynthesis builds up light elements: there is a very high O/Fe ratio. The O, Ne, Mg, Fe abundances are very sensitive to the progenitor mass.

As an example, SN 1006 (*Figure 16*) is a type Ia, 1000 yr old, SNR with angular diameter of 0.5° , distance of 2 kpc. X ray and radio emissions show two rims on the shell perpendicular to the magnetic field (polar caps). X ray flux is thermal in faint areas and synchrotron in bright rims. The interior shows thermal ejecta. As another example, DEM L71 is an SNR in the LMC, 5000 yr old. It shows typical LMC abundances. Central emission is seen above 0.7keV and $\text{Fe/O} > 5$ times the solar value. What happens there is that the reverse shock has heated all ejecta.

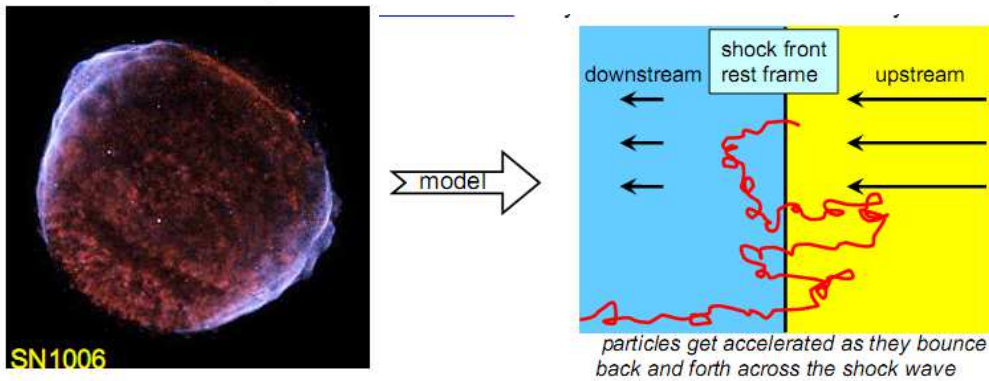


Figure 16: SN 1006 has been shown to accelerate particles across its shock front.

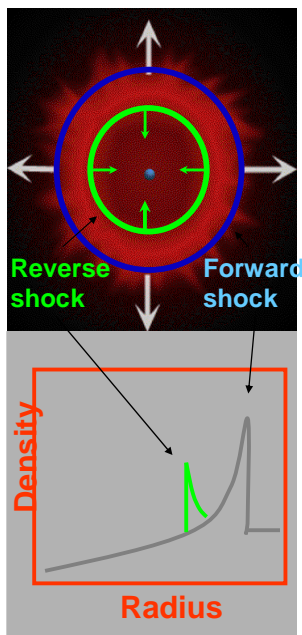


Figure 17: SNR shell structure.

One can this way understand the details of SNR shell structures (Figure 18). The explosion blast wave sweeps up the ISM in the forward shock. As mass is swept up, the forward shock decelerates and ejecta (having abundances as in the progenitor) catch up. Then, the reverse shock heats the ejecta and nuclear reactions produce new heavy elements. Once enough mass has been swept up ($> 1-5 M_{ej}$) the SNR enters the so called Sedov phase and slowly dilutes in the ISM.

While thermal particles and magnetic field are concentrated in the shell, relativistic particles extend to much larger distances and synchrotron emission is confined to magnetic field regions. The shock structure depends on the SNR age: one must

distinguish between young and old SNRs.

In the case of plerions (Figure 18), the situation is more complex: the pulsar wind sweeps up ejecta and the termination shock decelerates the flow, forming what is

called a pulsar wind nebula (PWN). The SNR sweeps up the ISM and the reverse shock heats ejecta, ultimately compressing the PWN.

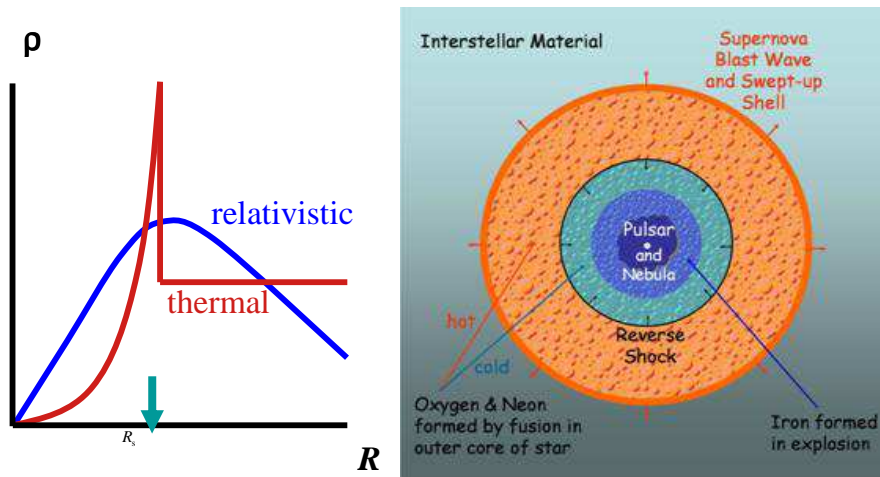


Figure 18: The plerion case.

2.4 Evidence for magnetic field amplification

There exists copious evidence in favour of strong magnetic turbulences and magnetic field amplification in the shock region of young SNRs. *Figure 19* shows the example of RX J1713 where X ray observations show a variable shock structure suggestive of strong turbulences and significant magnetic field amplification. Moreover important variations are also detected as a function of time, zones of turbulence becoming quiet and conversely on a few years time scale.

Moreover, features are observed in SNR shells which are suggestive of shock structures, as in SN 1006, or of non thermal filaments, like in Cass A. In the latter case, Chandra (*4 to 6 keV*), with a resolution better than *1 arcsec*, resolves the blast wave from the reverse shock.

Evidence for magnetic field amplification is obtained from the ratio of radio to TeV emission as a same distribution of electrons produces synchrotron (radio, X-ray) and TeV (Inverse Compton) photons but synchrotron depends directly on field while IC and pion decays do not.

The sharp outer X-ray edges seen in several young SNRs (Kepler, Cas A, Tycho, SN1006) provide additional evidence. Indeed, shock front compression is revelatory of field amplification. X-ray synchrotron emission from TeV electrons enhanced by strong field implies short electron lifetime and short diffusion lengths, hence narrow X-ray structures.

Magnetic fields are enhanced by factors of hundred, much larger than the factor of 4 associated with the compression factor of an ideal hydrodynamic shock. For example, in Cass A, one observes a front compression implying a magnetic field of $500 \mu G$ instead of the $10 \mu G$ expected otherwise (*Figure 20*).

Cosmic rays and the magnetized plasma carry similar energy densities: they do interact on each other. Accelerated particles tend to stream ahead upstream, which causes the generation of streaming instabilities and makes the evolution non linear, resulting in a strong amplification of the mean field: the structure of the shock is modified by cosmic ray retroaction. The higher field, in turn, depresses *Inverse Compton* with respect to synchrotron emission, implying faster scattering and increased maximum momentum.

Sharply peaked X-rays at forward shock are evidence that the field is large and increases sharply at the shock, and that diffusive shock acceleration is efficient and nonlinear at SNR outer blast wave shocks. Older remnants do not show such field amplification: The excitation of turbulences decreases with shock velocity, while damping (by non-linear wave interactions and ion-neutral collisions) does not.

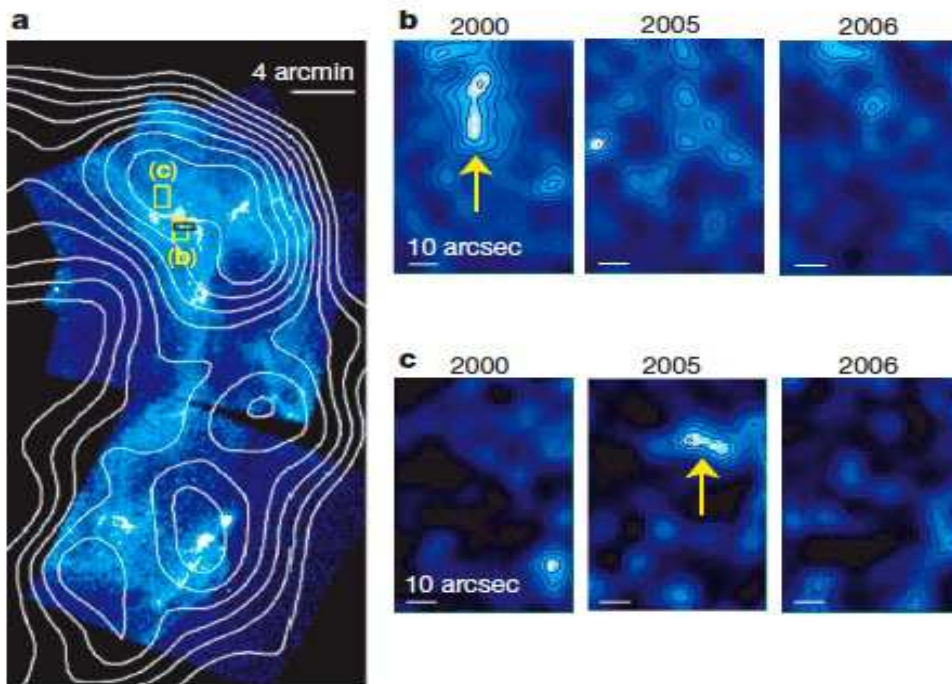


Figure 19: Evidence for time varying turbulences in the shell of RX J1713.

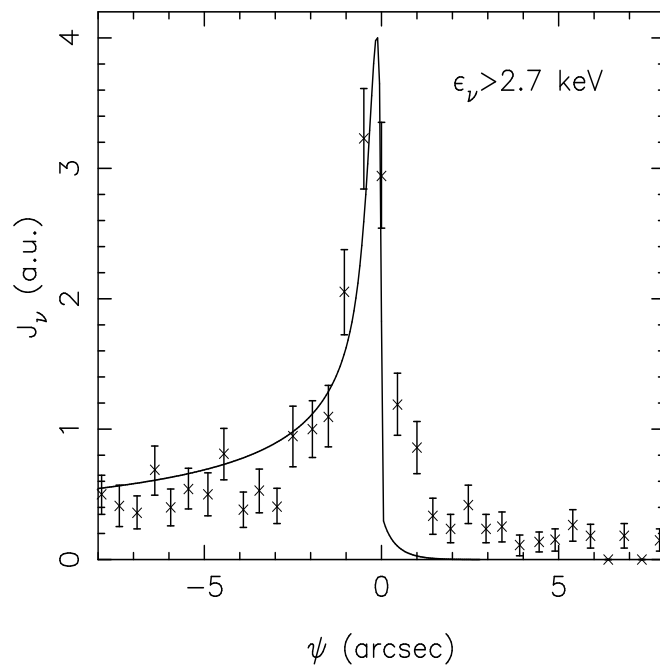


Figure 20: Field amplification in Cass A.

TYCHO (CHANDRA, 2005)

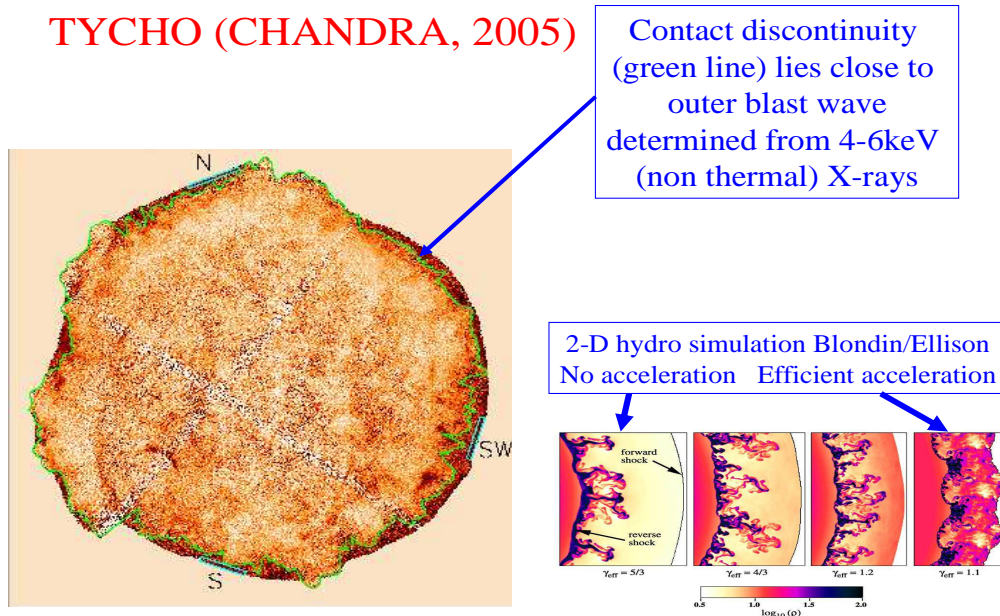


Figure 21: Magnetic amplification in Tycho.

Tycho (Figure 21) has been studied in detail by Chandra which found that the stellar debris are only half a light-year behind the outer shock instead of two expected, suggesting that a large fraction of the energy of the outward-moving shock wave is going into the acceleration of atomic nuclei (in addition to the electrons revealed by radio and X ray observations). Comparison with a simulation gives again evidence for strong magnetic field amplification.

2.5 Large scale shocks

SNRs are not large enough to be the sites of UHECR acceleration (see Hillas plot, Figure 12). As discussed earlier, AGNs and GRBs are more likely candidates. Indeed there exist many possible sites of large scale shocks (Figure 22). Galaxy collisions are one such example. Recent observations and studies of colliding galaxies

and merging galaxy clusters suggest that these were common phenomena in the early denser Universe. Such collisions are now believed to have played an important role in the process of galaxy formation. Galaxy collisions usually do not imply direct star collisions but the strongly increased gravity field enhances the collapse of hydrogen clouds and the formation of new stars, many of which very massive and therefore having a short life time.

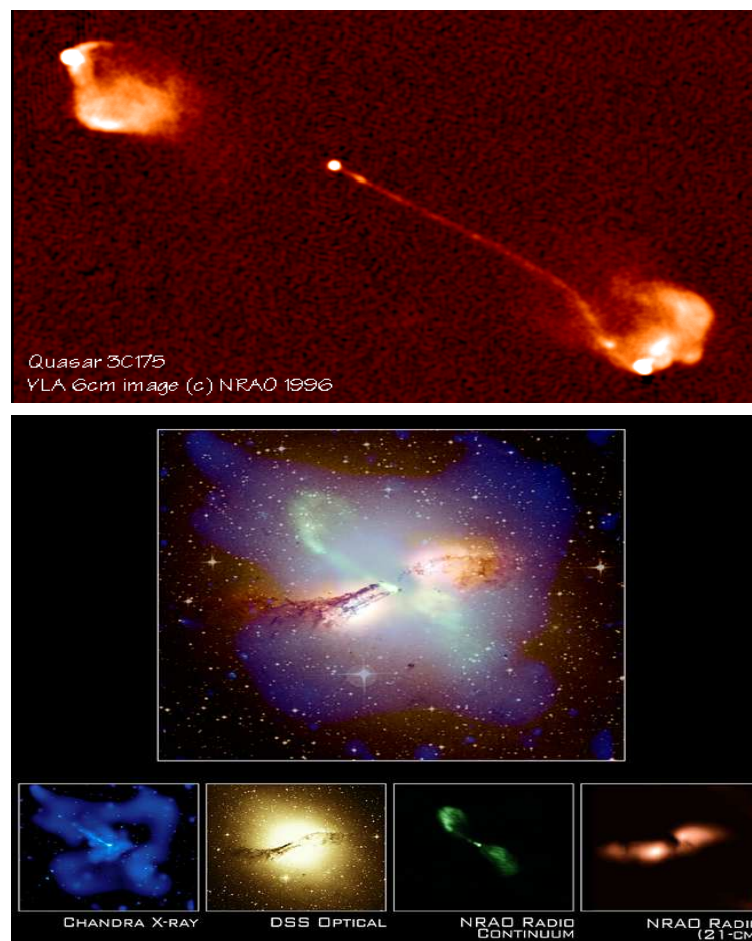


Figure 22. Up: Radio image of a quasar. Down: Centaurus A, merging of an elliptical with a smaller spiral, has an AGN in its centre (the AGN closest to us) and is the site of possible large scale shocks.

Galaxy collisions are sites of very violent events on large scales and are therefore most probably sites of large shocks. AGNs also, in particular their jets, are possible sites for UHECR acceleration. The observations made at the Pierre Auger Observatory in the years to come will enable the identification of the preferred acceleration sites.

CHAPTER 3

DIFFUSIVE SHOCK ACCELERATION

3.1 Hydrodynamic shocks

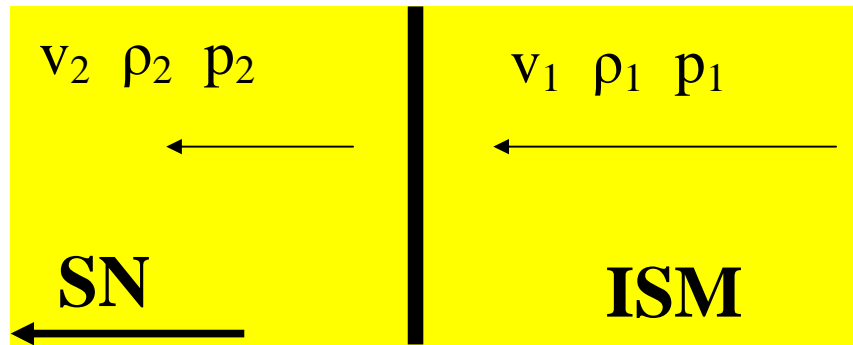


Figure 23. Definition of variables (the shock front is at rest).

Let us first recall the basic features of ideal hydrodynamic shocks (no magnetic field). We work in the shock frame (where the shock front is at rest) and use index 1 for upstream and index 2 for downstream, ρ are densities, v are velocities and p are pressures (Figure 23).

In the shock frame mass conservation gives $\rho_1 v_1 = \rho_2 v_2$, momentum conservation gives $\rho_1 v_1^2 + p_1 = \rho_2 v_2^2 + p_2$ and energy conservation gives (for an ideal gas) $\rho_1 v_1 (\frac{1}{2} v_1^2 + \gamma p_1 / \rho_1 / [\gamma - 1]) = \rho_2 v_2 (\frac{1}{2} v_2^2 + \gamma p_2 / \rho_2 / [\gamma - 1])$ where γ is the adiabatic index defined as $\gamma = C_p / C_v = (\alpha + 1) / \alpha$; here C_p and C_v are the specific heats for constant pressure and volume respectively and α is the number of degrees of freedom divided by 2 (3/2 for monatomic gas, 5/2 for diatomic gas). The equation for an ideal fluid undergoing a reversible (i.e., no entropy generation) adiabatic process is $pV^\gamma = cte$ where V is the specific or molar volume. For a monatomic ideal gas, $\gamma = 5/3$. For reversible adiabatic

processes, it is also true that $p^{\gamma-1}T^{-\gamma}=cte$ and $VT^\alpha=cte$ where T is an absolute temperature.

The sound velocity is $v_s = \sqrt{(\gamma p/\rho)}$ and $M=v/v_s$ is the Mach number.

From the three conservation equations (mass, momentum and energy), we have (see Appendix 1)

$$v_2/v_1 = (\rho_2/\rho_1)^{-1} = (\gamma-1+2M_1^{-2})/(\gamma+1)$$

$$T_2/T_1 = \{2\gamma M_1^{-2} - (\gamma-1)(\gamma-1+2M_1^{-2})\}/(\gamma+1)^2$$

The density ratio, $r=\rho_2/\rho_1$, is called the compression ratio. For large enough Mach numbers, $r = (\gamma-1)/(\gamma+1)=4$ for monatomic gases.

3.2 Astrophysical shocks

Astrophysical shocks are collisionless, as for example SNR shocks (where typically a solar mass is ejected at a velocity of a few percent of the light velocity) or interplanetary shocks induced by fluctuations of the solar wind. The arguments of the previous paragraph on hydrodynamic shocks might therefore sound irrelevant. Yet, in collisionless shocks as in hydrodynamic shocks, mass, momentum and energy must be conserved. But the calculations made above for hydrodynamic shocks use concepts that are not trivially applicable to collisionless shocks: ideal gases, adiabatic index, etc... Indeed, in the hydrodynamic case, collisions between atoms are responsible for the transformation of part of the upstream kinetic energy in downstream heat: when crossing the shock, temperature increases and velocities decrease. However, in a collisionless shock, the interaction between particles is mediated by magnetic fields (that are themselves induced by the particles, cosmic and thermal) and it is far from obvious that hydrodynamic arguments still apply.

In practice, however, the collisionless situation is far more complex than the idealized hydrodynamic situation presented in the previous paragraph might have

suggested. In particular, magnetic waves are induced in the plasma by the accelerated cosmic rays and modify their movement: there is an interaction between the flux of cosmic rays and the plasma waves. Of particular relevance is the ratio between the velocity of the particles and that of the plasma waves (Alfvén waves) and the occurrence of resonances.

Such nonlinear processes occurring in strong supernova shocks are currently the subject of numerous studies that are well beyond the scope of the present work. In particular V.S. Ptuskin and V.N. Zirakashvili (2005) have studied the instability in the cosmic-ray precursor of a supernova shock. They find that the level of turbulence in this region determines the maximum energy of accelerated particles, which strongly depends on the age of the SNR. The average spectrum of cosmic rays injected in the interstellar medium in the course of adiabatic SNR evolution takes the approximate form E^{-2} at energies larger than 10 to 30 GeV/nucleon with a maximum close to the position of the knee.

3.3 Acceleration by successive shock traversals

We repeat the calculation of Section 2.1 in the simple case of a magnetic field wall of intensity B (Figure 24). Two successive Lorentz transformations give:

$$E^* = \gamma E_{in} - \gamma \beta p_{zin} \quad p_z^* = -\gamma \beta E_{in} + \gamma p_{zin}$$

$$E_{out} = \gamma E^* - \gamma \beta p_z^* \text{ since both } \beta \text{ and } p_z^* \text{ change sign.}$$

$$\text{Hence } E_{out} = \gamma^2 (1 + \beta^2) E_{in} - 2\gamma^2 \beta p_{zin}$$

$$\text{As } p_z = p \cos \theta \text{ and } p/E = \beta_{CR}, \text{ one finds for } \beta \ll 1 \text{ } (\gamma = 1),$$

$$\Delta E = E_{out} - E_{in} = -2\beta p_{in} \cos \theta$$

$$\Delta E/E \sim -2 \beta \beta_{CR} \cos \theta$$

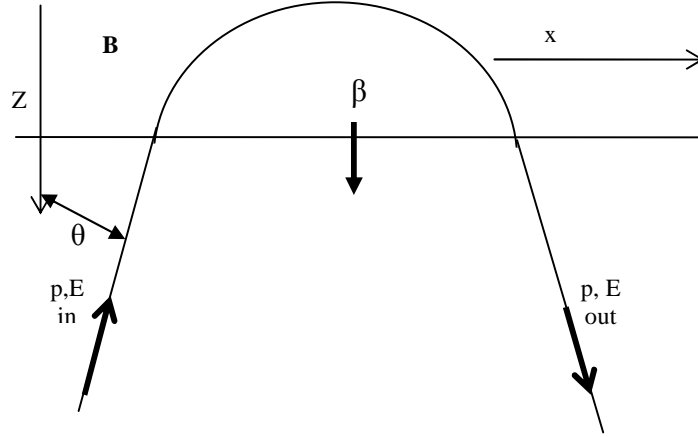


Figure 24: definition of variables.

where, $\Delta E/E$ is the relative energy gain, β_{CR} the cosmic ray velocity (in units of light velocity), β the relative velocity of the two media ($\beta=v_1-v_2$) and θ the angle of incidence on the wall ($=0$ for normal incidence, it is the same when going in or coming out). It is an energy gain when the two β 's have opposite sign, that is when the cosmic ray and the magnetic wall aim at each other (which is always the case for relativistic cosmic rays). It may sound strange to have acceleration without electric field but, of course, the Lorentz transformation does induce an electric field, which produces the acceleration.

$\Delta E/E \sim -2 \beta \beta_{CR} \cos\theta$ is the basic equation of diffusive shock acceleration. Real magnetic field configurations are very different from the ideal case considered here (indeed a magnetic bottle might have been closer from concrete configurations) but the result is qualitatively always the same. ○

As the shock progresses into the unperturbed ISM the density increases suddenly by a typical factor of $r=\rho_2/\rho_1 \sim 4$ and the temperature increases by a factor $T_2/T_1 \sim 1/3 M_1^2$. On either side of the shock one sees the other medium approach at a

velocity v_1-v_2 and a relativistic cosmic ray crossing the shock at an angle θ gets always a first order Fermi acceleration, $\Delta E/E \sim 2(v_1-v_2)\cos\theta$.

Writing $(v_1-v_2) = 3v_1/4$, one finds the number of particles per unit volume having a velocity in a solid angle $d\Omega(\theta)$ around θ $dn(\theta) = n_0 d\Omega(\theta)/4\pi = 1/2n_0\sin\theta d\theta$. Their velocity with respect to the front is $v\cos\theta$ and their flux across the front is $1/2n_0v\cos\theta\sin\theta d\theta$. Averaging $\cos\theta$ over such a $\cos\theta\sin\theta$ distribution gives $\langle\cos\theta\rangle \sim 2/3$ when crossing the front from upstream and $\langle\cos\theta\rangle \sim -2/3$ when crossing the front from downstream. Hence, for two successive traversals, $\Delta E/E \sim 4\beta/3$. Here β stands for the relative velocity between the two media, which is $(r-1)\beta_{shock}/r$. For $r=4$, the relative energy gain is therefore $\Delta E/E \sim \beta_{shock}$.

3.4 Energy spectrum

The rate of acceleration is given by the ratio of the relative energy gain when crossing the shock back and forth, $\Delta E/E \sim \beta_{shock}$, to the time Δt it takes. In the relativistic limit and in the approximation where the distribution of the scattering centres is irrelevant, the length of a trajectory is proportional to momentum, or equivalently time is proportional to energy, $\Delta t = kE$ where k is related to the diffusion coefficients in the upstream and downstream media. Once in region 1, the particle will always be caught by the shock, which is aiming toward it. However, once in region 2, it may escape the shock region forever with a probability P_{esc} . In this region, the scattering centres move away from the shock at velocity $v_2 \sim 1/4v_{shock}$ while the particle moves at light velocity at varying angles to the shock. Integrating over these angles, we get $P_{esc} = 4\beta_{shock}/r$.

Having now the three relations: $\Delta E/E \sim [4(r-1)/3r]\beta_{shock}$, $\Delta t = kE$ and $P_{esc} = 4\beta_{shock}/r$ we find that after n cycles across the shock,

$E_n = E_0(1 + [4(r-1)/3r]\beta_{shock})^n$. At each cycle only a fraction $(1 - P_{esc}) = (1 - 4\beta_{shock}/r)$ survives. Hence after n cycles one has $N = N_0(1 - 4\beta_{shock}/r)^n$ particles having energy in excess of $E = E_0(1 + [4(r-1)/3r]\beta_{shock})^n$.

Replacing $n = \ln(E/E_0)/\ln(1 + [4(r-1)/3r]\beta_{shock})$ and noting that $x^{\ln y} = y^{\ln x}$,

$$N = N_0(1 - 4\beta_{shock}/r)^n = N_0(E/E_0)^w \text{ with } w = \ln(1 - 4\beta_{shock}/r) / \ln(1 + [4(r-1)/3r]\beta_{shock})$$

Taking the derivative with respect to energy one obtains the differential energy spectrum which is a power spectrum of index $w-1$. To first order in β_{shock}

$$w = -3/(r-1) \text{ and } w-1 = -(r+2)/(r-1) \text{ which reduces to } -2 \text{ for } r=4.$$

Diffusive shock acceleration results in a universal power law energy distribution with an index close to reality (the value 2.7 of the cosmic ray index is increased by interactions of the cosmic ray with the ISM; removing this effect yields a lower value, between 2 and 2.5).

CHAPTER 4

A SIMPLE SIMULATION

4.1 General framework

In order to become familiar with the process of diffusive shock acceleration and to understand its main features, a simple simulation has been written. The basic code is listed in Appendix 2.

The front is taken to be planar and progresses at velocity β_{front} in the ISM. Typically, we are dealing with an SNR having expanded at 1% of light velocity for 1 kyr, meaning a radius of some 10 light years, some 10% of the final radius before entering the Sedov phase and dissolving in ISM. We shall deal with magnetic fields of up to 1 mG, namely up to 10^{-7} T. Over a distance of 10^9 m, or ~ 3 light seconds, the transverse momentum kick is therefore up to ~ 30 GeV.

The x axis is taken normal to the front pointing upstream (meaning toward the undisturbed ISM). Space is divided in cells of equal sizes. Units of length or time ($c=1$) are *seconds*, of momentum or energy ($\hbar=1$) are *GeV* and of magnetic field are μG . One unit of field over one unit of distance means a transverse momentum kick of 9 MeV, i.e. 0.009 units of energy. For a field of $H \mu G$ over a distance of l light seconds, a particle of momentum p GeV gets a transverse momentum kick of $\Delta p = 0.009 H l$. Its Larmor radius is $R = 111 p/H$.

The program tracks particles (assumed to be protons) with a step of 0.03 Larmor radii, that is $3.33 p/H$. The momentum is followed typically from 1 to 1000 GeV, meaning Larmor radii between 0.33 and 333 light seconds for a 10 μG field. Cell sides are accordingly chosen to be one light second. Field irregularities of the same scale are generated by locating a magnetic dipole in the centre of each cell.

Calculations are performed in the frame of the medium in which the particle happens to be. This means that a Lorentz transformation is made at each front traversal. Upstream, one sees the shock approach at a velocity β_{front} and downstream one sees the shock moving away at a velocity of $0.25\beta_{front}$ under the assumption that the compression ratio is 4, as obtained for monatomic gases in hydrodynamics. In each frame, upstream or downstream, one sees the other medium approach at a velocity $0.75\beta_{front}$.

4.2 Magnetic field

Space is divided in cells of sides equal to *1 light second*. The magnetic field is given in $100 \times 50 \times 50$ cells surrounding the origin. In each cell one gives the value of a mean field (constant over the cell) and that of the magnetic moment of a magnetic dipole located at the centre of the cell. In any given point, the magnetic field is calculated as the sum of the mean field in the cell containing the point and of the twenty-seven dipole fields of the twenty-seven cells surrounding the point.

We recall that the field (*Figure 25*) at a vector distance \mathbf{r} from a dipole magnetic moment \mathbf{M} is, up to a constant factor, $\mathbf{H} = (3\mathbf{r}(\mathbf{M} \cdot \mathbf{r}) - \mathbf{M}r^2)/r^5$.

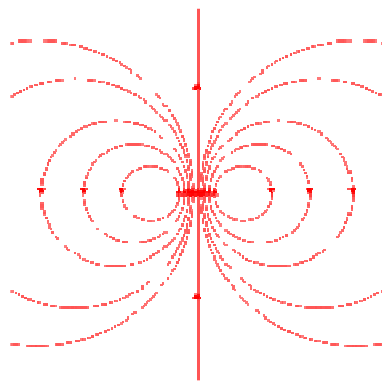


Figure 25. Dipole field.

At unit distance along the magnetic moment, \mathbf{H} is also directed along the magnetic moment and equal to $2\mathbf{M}$. At unit distance in the equatorial plane, \mathbf{H} is directed against the magnetic moment and equal to $-\mathbf{M}$. A dipole field is the field generated by a current loop in the approximation where the loop radius can be neglected. Indeed, \mathbf{H} as given above diverges at $r=0$. In the case of a current loop, the real field differs from the dipole field at distances to the centre at the scale of the

loop radius. In order to obtain a realistic field shape, it is therefore necessary to replace the dipole field by another expression when approaching the centre. In the present simulation, the field is taken to be the dipole field outside and on a sphere of radius 0.5. Inside the sphere, the field is linearly interpolated between the value on the sphere at the intersection with the line joining the point to the centre and the central value obtained with a current loop of magnetic moment \mathbf{M} . A current loop of radius R and current I has $M=\pi IR^2$ pointing along the loop axis and the field in the centre is, up to the same constant factor as above, $2\pi I/R=2M/R^3$. Taking the loop around the sphere equator gives a field equal to $16M$ in the centre of the loop. The field on the sphere is $8(3\check{\mathbf{r}}(\mathbf{M}\cdot\check{\mathbf{r}})-M)$ where $\check{\mathbf{r}}$ is the unit vector along \mathbf{r} . The interpolation goes therefore between $16M$ and $-8M$ in the equatorial plane; along the dipole axis, the field stays constant and equal to $16M$.

4.3 Uniform magnetic field

In order to get some familiarity with the main features of the process, it is useful to start looking at the simple case of a uniform magnetic field. As it is the components of the magnetic field parallel to the front that cause front traversals, it is sufficient to consider a magnetic field H directed along z . Proton trajectories are helices projecting as circles in the (x,y) plane. There is no loss of generality by assuming that the initial proton momentum is in the (x,y) plane, implying circular trajectories. *Figure 26* shows the trajectory¹ of a relativistic proton starting upstream with a momentum $p_0=E_0=10$ GeV in a field $H=500\mu G$. Its radius is therefore $R_0=2.2$ s. The initial position of the proton is taken to be $x_0=5$ s away from the front, such that the initial circular trajectory does not cross the front. The closest distance of approach to the front depends in a

¹ Note that what is plotted in *Figure 26* and following is not in real space but in the rest frame of where the particle happens to be. Namely the front stays at $x=0$ and both the upstream and downstream trajectories are drawn in half-spaces that are at rest.

trivial way from the orientation of the initial momentum: if it is normal to the front, whether it points away from it or towards it, the distance of closest approach is $5.0 s - 2.2 s = 2.8 s$: the centre of the circle is at the same distance from the front as the initial proton. If it is parallel to the front and pointing against y the circle is completely contained upstream of the starting point and the distance of closest approach is therefore $5s$. If it is pointing along y the circle is completely contained downstream of the starting point and the distance of closest approach is therefore $5.0s - 4.4s = 0.6s$.

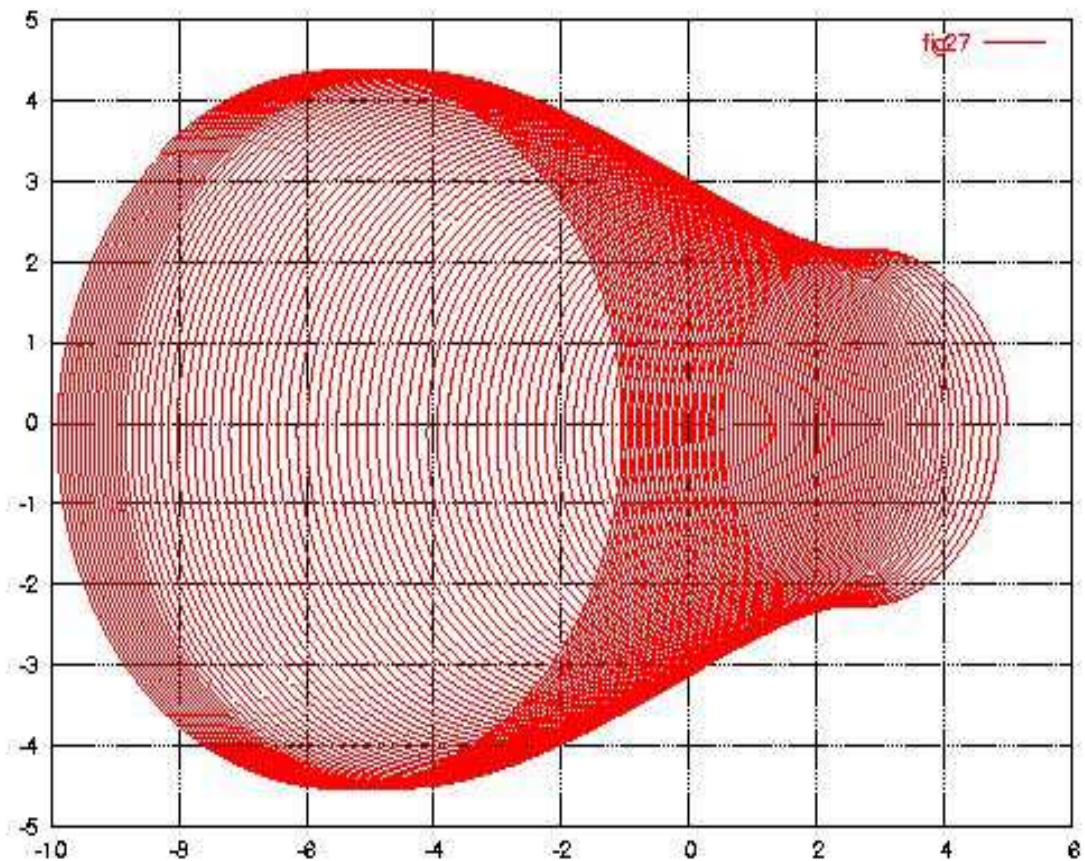


Figure 26. Trajectory of a particle accelerated in a uniform magnetic field (see text). From right to left one can see successively a drift toward the front, acceleration across the front and a drift downstream.

It takes $2\pi R_0=13.8$ s for the proton to go around. The trajectories displayed in *Figure 26* are for a front velocity $\beta_{front}=0.01$. When the proton has made a turn, the front has therefore approached by 0.138 s. When the distance of closest approach is 0.6 s, it takes therefore $0.6/0.138=4.3$ turns before the first front crossing. During this time, the proton energy remains constant and equal to 10 GeV.

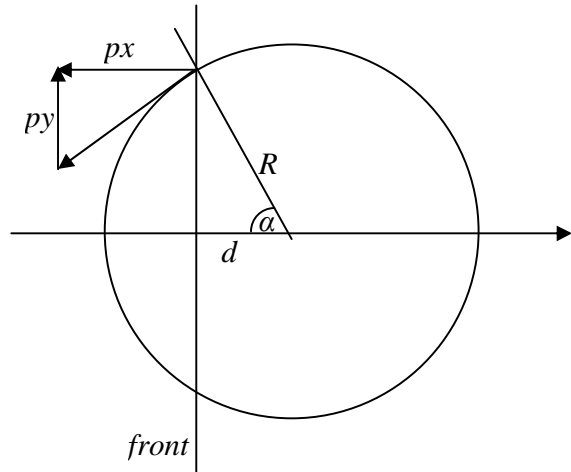


Figure 27. Uniform field geometry

After completion of this initial phase of approach, the trajectory crosses the

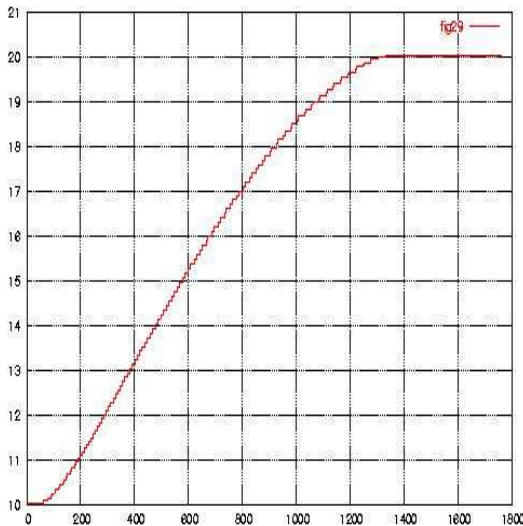


Figure 28. Dependence of energy on time for the trajectory of Figure 27 (uniform magnetic field).

front, twice per turn. Calling $d=-R\cos\alpha$ the distance from the centre of the circle to the front (*Figure 27*), α varies from 0 to π and d from $-R$ to R while the front scans through the circle. The relative energy gain per turn is proportional to the x component of the momentum, namely $\Delta E/E=2\sin\alpha\times 0.75\beta_{front}$. The radius of the trajectory accordingly increases by the same relative amount at each turn, $\Delta R/R=\Delta E/E=1.5\sin\alpha\beta_{front}$. At crossing, as $d/R=p_y/p=\cos\alpha$, $d=p_y R/p=cte$. Indeed, p_y is invariant and

so is the ratio R/p . At each new crossing, R , p and p_x all grow but d remains constant. Hence $\Delta d=0=-\Delta R \cos \alpha+R \sin \alpha \Delta \alpha$ and $\Delta \alpha=1.5 \cos \alpha \beta_{front}$. The angle α first grows when the front is downstream the centre of the circle and then decreases when the front is upstream.

After crossing, R stays constant but d starts increasing: the particle spends a time $2R\alpha$ in the downstream region or $2R(\pi-\alpha)$ in the upstream region; each full turn, the front advances by $\Delta d=2R\beta_{front}(0.25\alpha+\pi-\alpha)$
 $=2R\beta_{front}(\pi-0.75\alpha)$ with respect to the particle trajectory. As R is now constant, $\Delta d=R \sin \alpha \Delta \alpha$ and $\Delta \alpha=\Delta d/(R \sin \alpha)=2\beta_{front}(\pi-0.75\alpha) / \sin \alpha$.

Therefore, at each turn, α increases by $1.5 \cos \alpha \beta_{front}$ when crossing the front and by $2\beta_{front}(\pi-0.75\alpha) / \sin \alpha$ when circling around. Hence

$$\Delta \alpha / \beta_{front}=1.5 \cos \alpha+2(\pi-0.75 \alpha) / \sin \alpha$$

$$\Delta E / E=1.5 \sin \alpha \Delta \alpha / \{1.5 \cos \alpha+2(\pi-0.75 \alpha) / \sin \alpha\}$$

Writing $F(\alpha)=\int 1.5 \sin x dx / \{1.5 \cos x+2(\pi-0.75 x) / \sin x\}$ where the integral runs from 0 to α , the particle energy is $E=E_0 \exp (F(\alpha))$. When the front has scanned through the trajectory, the particle energy has increased by a universal factor² $\exp (F(\pi))=2$: as long as the first trajectory is upstream and does not cross the front, it will always ultimately drift fully downstream and the energy will have doubled independently from the values of the magnetic field, of the front velocity and of the initial momentum.

After the acceleration phase, the proton stays on its fixed circular orbit in the downstream region while the front keeps drifting away. *Figure 28* shows the dependence of energy on time.

² Indeed, the integrand reads du/v with $v=0.75(2 \cos x \sin x-2 x)+2 \pi=0.75(\sin 2 x-2 x)+2 \pi$ and $du=1.5 \sin ^2 x=0.75(1-\cos 2 x)$. Hence $du=-dv/2$ and $F(\alpha)=\{(\log v)_{\alpha=0}-(\log v)_{\alpha=\pi}\} / 2$. Hence $E / E_0=\exp (F[\pi])=\sqrt{\{(v)_{\alpha=0} / (v)_{\alpha=\pi}\}}=\sqrt{\{2 \pi /(\pi / 2)\}}=\sqrt{4}=2$.

4.4 Lined-up dipoles

The preceding section has shown that a proton starting from upstream in a uniform magnetic field and with an initial momentum normal to the field will always end up being accelerated, however by a very small factor of only 2 independent of its initial momentum, of the amplitude of the magnetic field and of the velocity of the front.

One might expect that fluctuations in the magnetic field could occasionally allow for stronger accelerations. In order to explore this possibility, we first consider a field generated by a set of parallel dipoles located at the centre of each cell and having a common magnetic moment of $30 \mu Gs$ directed along z . The field in the centre of each cell is therefore $30 \times 16 = 480 \mu G$, similar to the uniform field of the previous paragraph. We generate 100 trajectories by choosing the starting point at random in the cell $x \in [3,4]$ and $y \in [0,1]$, $z=0$, the momentum being $(0,10, 0)$ as in the previous case. Trajectories are followed for 150'000 steps and in only one case does the energy exceed 20 GeV. The associated trajectory and energy dependence on time are illustrated in *Figure 29*. The trajectory remains confined around the front and drifts only slowly in the positive z direction, which has of course no incidence on acceleration. While the exercise demonstrates that it is now possible to exceed the factor 2 in acceleration, it also shows that it takes a much longer time, 40'000 instead of 1'300 s. Moreover, most trajectories escape the front without having been much accelerated. Another interesting feature of the trajectory displayed in *Figure 30* is that acceleration would continue if one allows for more time: indeed, going to 300'000 steps brings the energy up to ~ 25 GeV as shown in *Figure 30*.

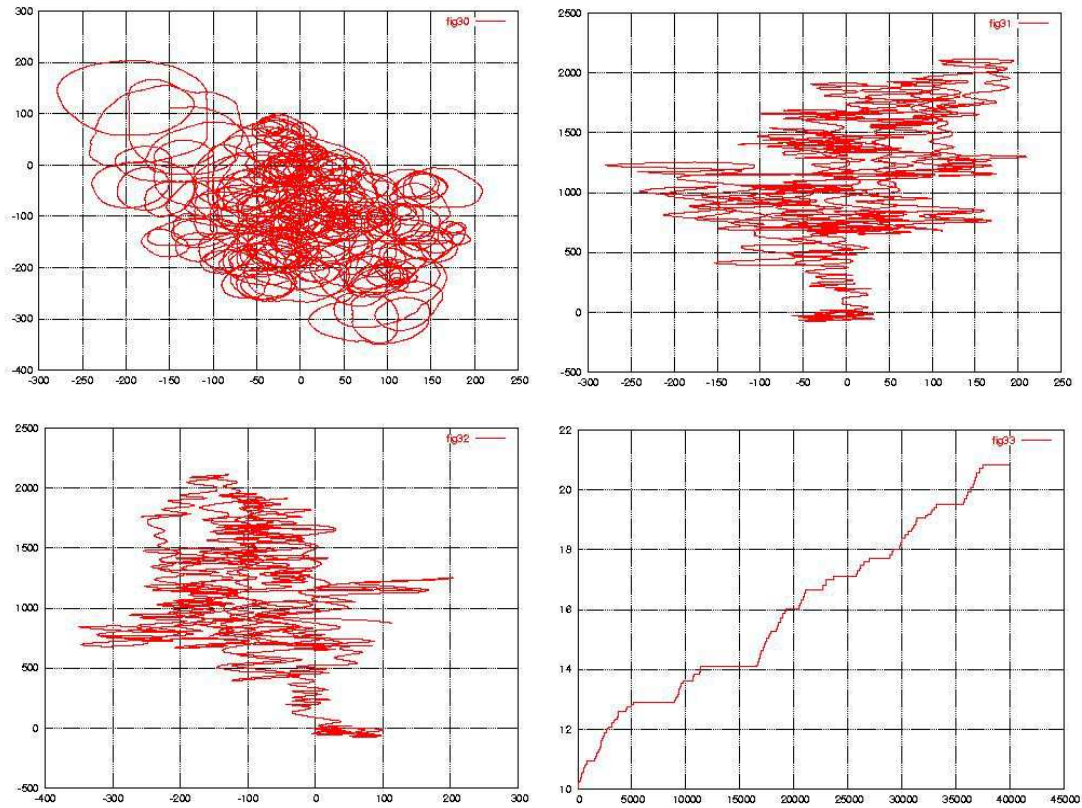


Figure 29. Trajectories of a particle being accelerated by more than a factor 2 in the lined-up dipole configuration. From left to right and from top to bottom: (x, y) , (x, z) and (y, z) projections followed by the dependence of energy on time.

4.5 Random dipoles

4.5.1 Generalities

Having established that space fluctuations in the magnetic field allow for reaching larger accelerations than with a uniform field, we now undertake a systematic study of the effect, this time describing the magnetic field as a superposition of a uniform field H_0 along the z axis and of dipoles having a common magnetic moment

M_0 and random orientations. By changing the values of H_0 and M_0 it is then possible to learn about their relative roles.

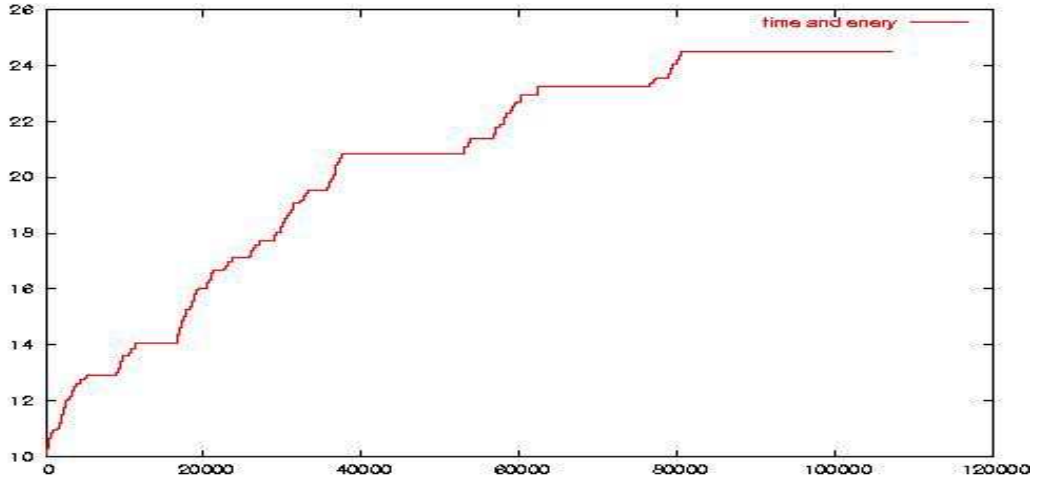


Figure 30. Dependence of energy on time for the event displayed in Figure 29 (lined-up dipoles). The time scale expands farther away than in Figure 29.

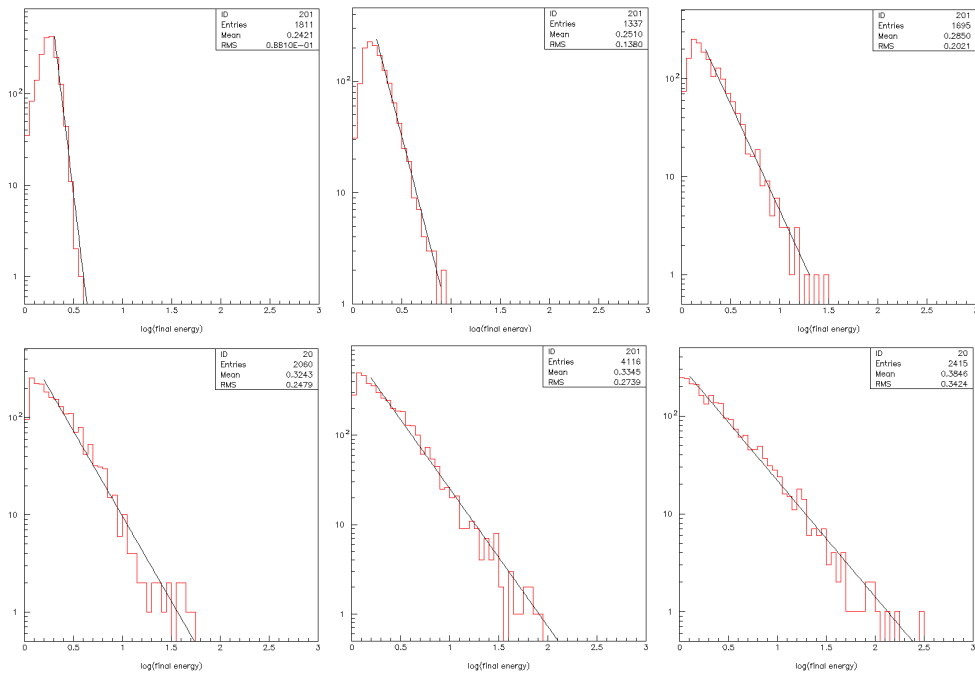


Figure 31. Distributions of $\log_{10}(E/E_0)$ obtained for $H_0=250$ and values of M_0 increasing from 5 to 50 (see Figure 32).

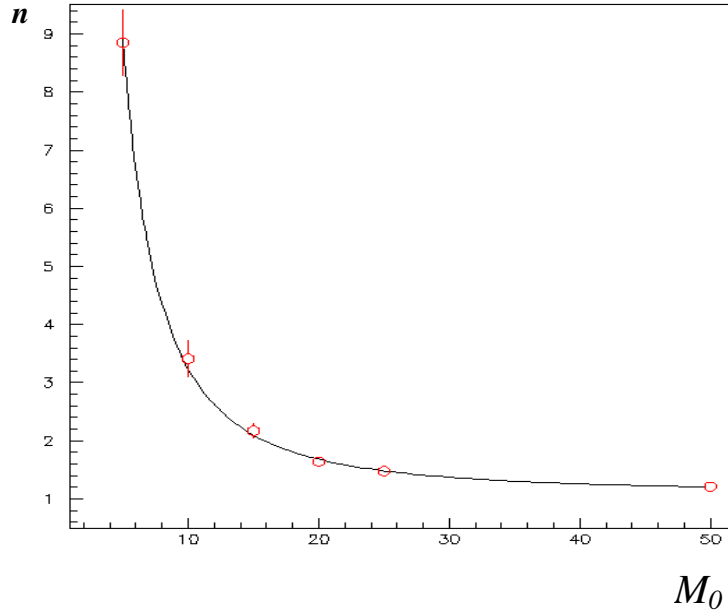


Figure 32. Dependence of the index n on the amplitude M_0 of randomly oriented dipoles for $H_0=250$, $\beta=2\%$ and an initial momentum of $10 \text{ GeV}/c$. The line is the result of a fit of the form $n_0+(k/M_0)^p$ with $n_0=1.10\pm 0.05$, $k=15.0\pm 0.8$ and $p=1.88\pm 0.10$.

In each field configuration a sample of at least 1000 particles is followed until the particles escape in the downstream region at such a distance that they have no chance to return to the front. The initial positions of the particles are chosen at random in the upstream region. The initial momentum p_0 is taken to be 10 GeV , which implies for the initial energy $E_0 \sim p_0$. The front velocity is taken to be 2% of the light velocity.

Figures 31 and 32 illustrate the role played by the random dipoles in the acceleration for $H_0=250$ and various values of M_0 . The energy distributions (shown in log-log scale) are compared with a power law, $dN/dE \sim E^{-n}$. The evolution from the uniform field case (no perturbations), where the final energy is exactly twice the initial energy, to the asymptotic regime ($n \sim 1$) is completed for $M_0 \sim 50$ as can be seen in Figure 32. Lower dipole amplitudes are associated with energy distributions that are not well described by a power law and are prematurely cut off (Figure 31). The error

bars shown in *Figure 32* are the result of the power law fits, restricted to intervals where they apply, but the true systematic errors may be somewhat larger.

The results of a systematic study of the dependence of the energy spectrum on the magnetic field are illustrated in *Figure 33*. In all cases, the front velocity is 2% and the initial particle momentum is 10 GeV. It shows the energy spectra obtained for different values of H_0 and M_0 . Each panel corresponds to a fixed value of H_0 and, in each panel, spectra associated with different values of M_0 are shown together. One observes that when M_0 increases, the energy distribution tends to a power law with index close to unity, the spectrum is being cut off at values that increase with M_0 .

We checked that the cut-off was not the result of too strict a definition of the stage at which the particle was judged to have no chance to return to the front: *Figure 34* compares the results obtained for $H_0=0$ using two different values of the downstream cut-off, 1000 light seconds and 2000 light seconds respectively.

We learn two lessons from *Figure 33*.

First, the dipole fluctuations must be large enough in comparison with the uniform field in order to have an effect. If they are too weak, they only slightly distort the circular trajectories and the particle drifts downstream without having a chance to return to the front. We see from *Figure 33* that, typically, M_0 must exceed something like $H_0/10$ for the fluctuations to be able to efficiently bring back the particle to the front. Second, the field amplitudes must be large enough to prevent the particle from escaping.

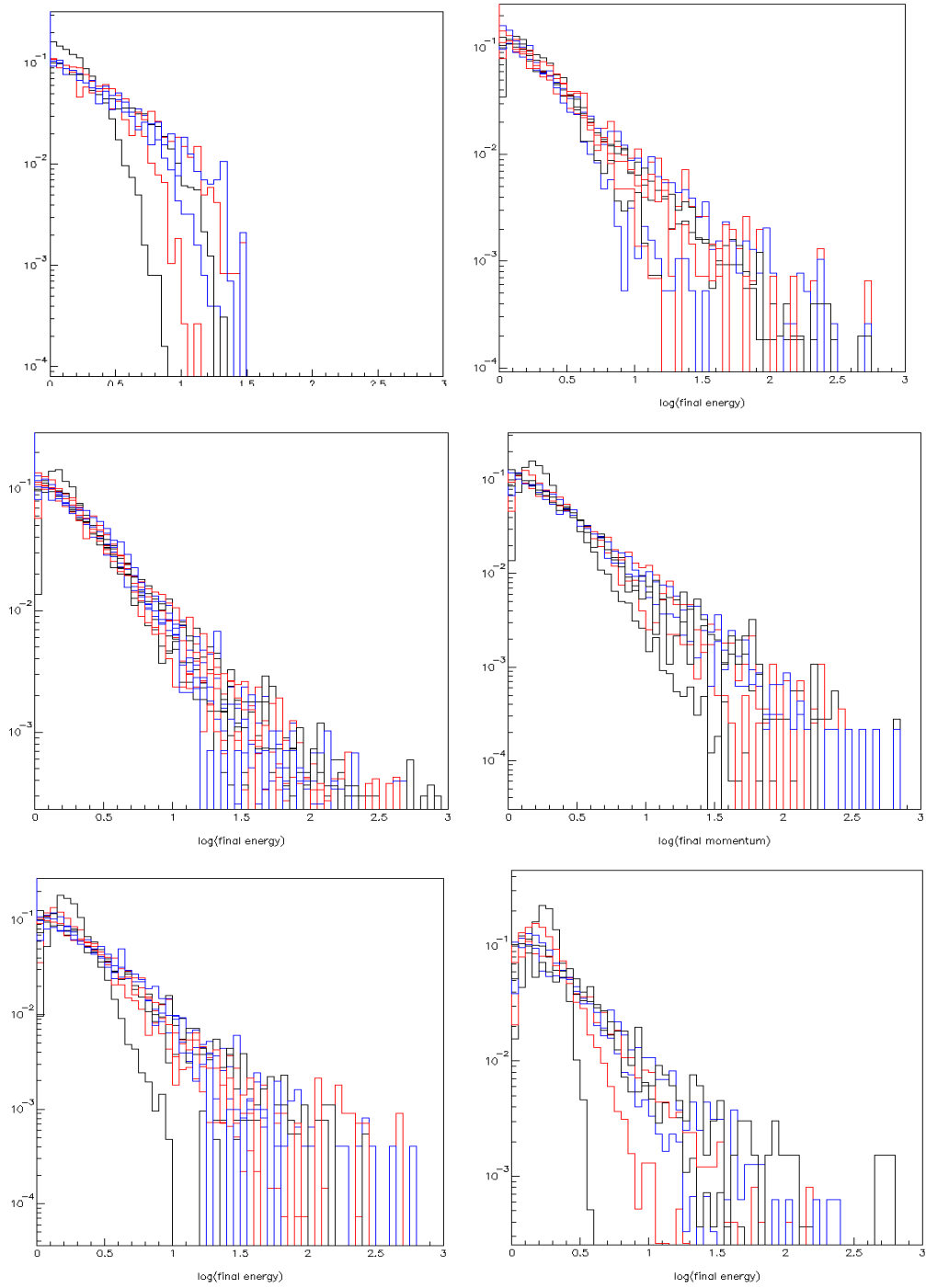


Figure 33. Distributions of $\log_{10}(E/E_0)$ for a magnetic field including a fixed component parallel to the z axis, H_0 , and randomly oriented dipoles having a common magnetic moment M_0 (from the list 5, 10, 15, 20, 25, 50, 75, 100, 150). From left to right and from top to bottom $H_0 = 0, 25, 50, 75, 100$ and 200 . The front velocity (in units of light velocity) is $\beta = 2\%$.

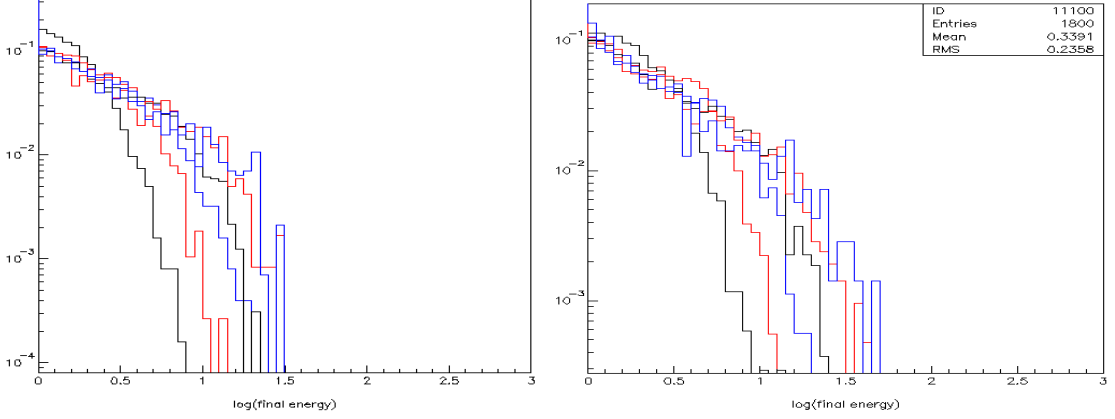


Figure 34: Comparison between the $H_0=0$ spectra obtained with a cut-off of 1000 light seconds (left panel) and respectively 2000 light seconds (right panel) downstream the front.

4.5.2 H_0 - M_0 resonance

Figure 35 shows typical trajectories of a particle having a Larmor radius of order unity ($H_0=1000$, $p_0=10$). For $M_0/H_0=1\%$ (left panel) the fluctuations are not sufficient to bring the particle back to the front: it drifts away downstream. For $M_0/H_0=100$ (right panel) the Larmor radius associated with the fluctuations is much smaller than that of the uniform field: the particle trajectory is locally a helix which displays characteristic magnetic mirror features, the particle being reflected when the pitch angle reaches 90° , as happens near the poles of the earth in the case of auroras. In between, for the central panel, and in particular for $M_0/H_0=10\%$ (central left panel) a good confinement is achieved.

A global survey of the relative roles of H_0 and M_0 is illustrated in Figure 36, which shows a map of $\rho = \langle \log_{10}(E/E_0) \rangle$, a parameter that measures the efficiency of the acceleration process, in the $\log_{10}H_0$ vs $\log_{10}M_0$ plane. It gives evidence for a

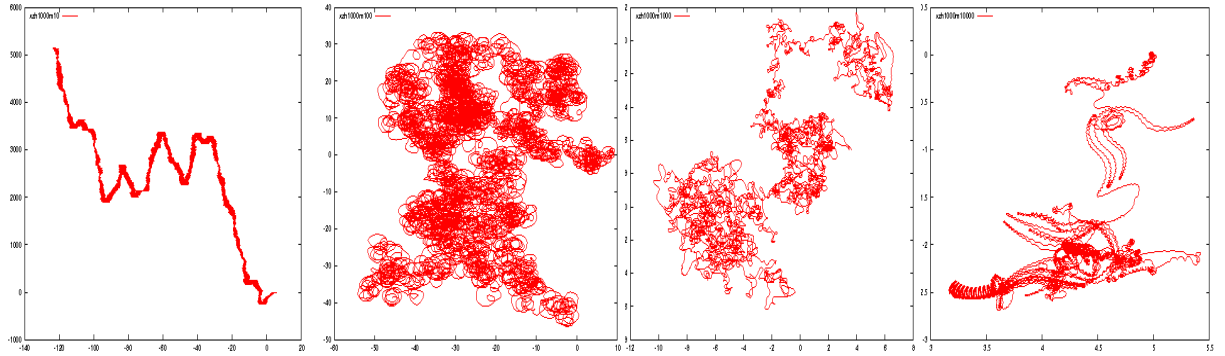


Figure 35. Trajectories in the (x,y) plane of a 10 GeV proton in a 1 mG field with added fluctuations such that $M_0/H_0=1\%$, 10%, 1 and 10 (from left to right).

favoured relation between H_0 and M_0 with M_0/H_0 increasing from ~ 0.2 to ~ 0.5 when H_0 increases from 10 to 10000. This relation corresponds to a kind of resonance between the respective roles of H_0 and M_0 . It was already apparent on Figures 31 and 33: for a given H_0 , when the M_0 scan is centred on the corresponding favoured value, as in the third panel of Figure 33, the acceleration is always efficient. On the contrary when M_0 is far from the favoured value, either too low as in the first panels of Figure 31 or too high as in the first panel of Figure 33, the acceleration stops prematurely. One can qualitatively understand the need for H_0 and M_0 to be commensurate in order to achieve a good acceleration. As already noted, if the fluctuations are too small they cannot sufficiently modify the circular trajectories and prevent them from drifting away downstream. The case where the fluctuations are too large is more subtle. In the absence of a uniform field component, the particle follows a random walk trajectory and will take much longer to return to the front than in the case of a uniform field where a single circle is enough. During that time, the front will have moved farther away than in the uniform field case. The optimum is a compromise where the fluctuations are sufficiently large in comparison with the uniform field to prevent the particle from drifting away and where the uniform field is sufficiently large for its

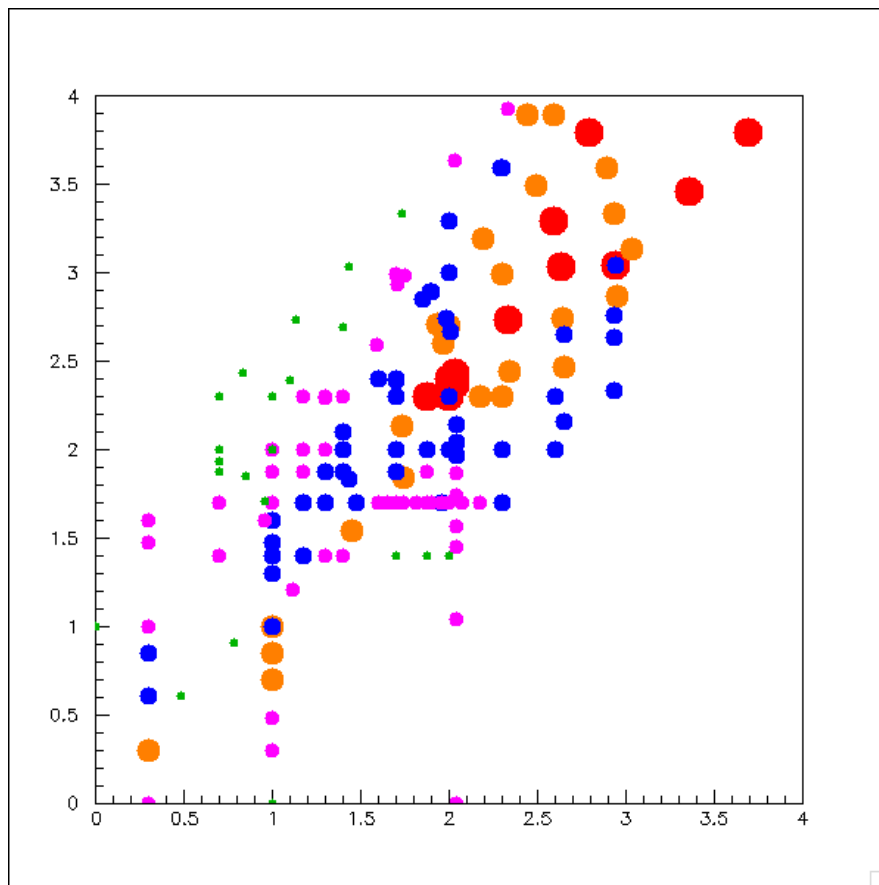


Figure 36. Distribution of ρ in the $(\log_{10}H_0, \log_{10}M_0)$ plane. The size of the dots increase with the value of ρ in the following intervals: <0.3 , 0.3 to 0.35 , 0.35 to 0.4 , 0.4 to 0.425 and >0.425 .

coherent action to help bringing the particle back to the front more efficiently than a random walk would.

4.5.3 R-D relation and scaling.

The ratio between M_0 and H_0 is not the only relevant parameter. The amplitudes of the fields are equally important. Having understood the former, we now study the

effect of the latter. *Figure 37* illustrates the dependence of ρ on M_0 when $H_0=0$. In that case, as can be seen from *Figure 33*, the slope of the energy spectrum is small, resulting in relatively large ρ values, but the spectrum is prematurely cut-off. The acceleration is more and more efficient as M_0 increases. Such an improvement is seen

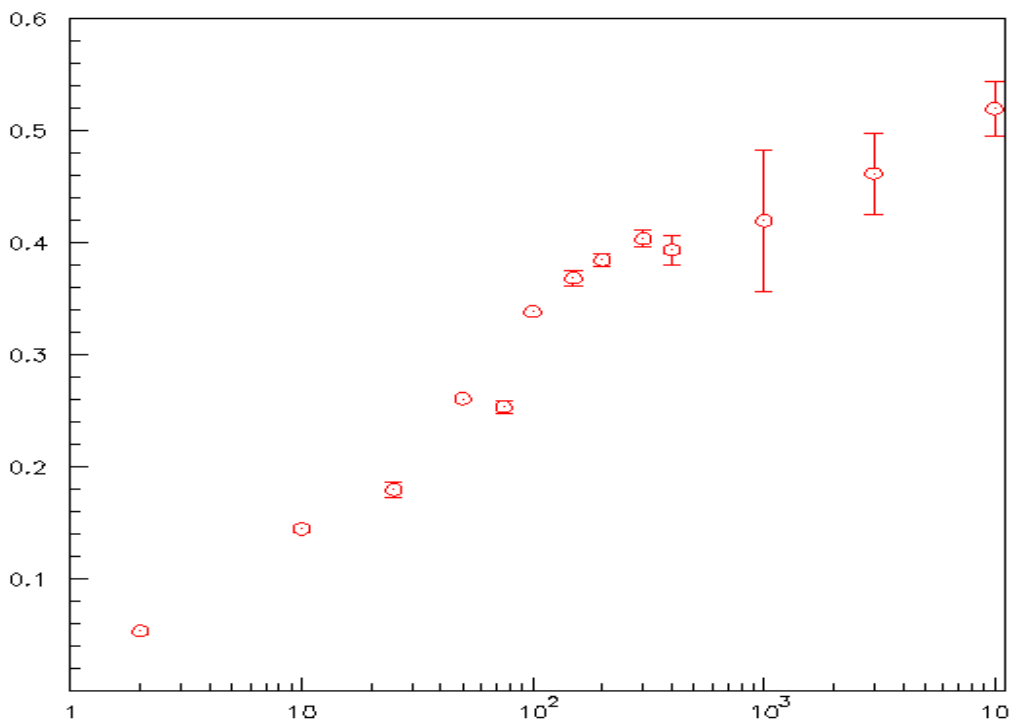


Figure 37. Dependence of ρ on M_0 for $H_0=0$.

to occur for other values of H_0 , as is apparent from *Figure 36*. One may then wonder how far this improvement of the acceleration efficiency can go. However, to answer this question, one cannot keep increasing the amplitude of the fields beyond reason, say a few milligauss at the very most (we recall that 1 mG is one thousand of the units being used here). What is done instead is to exploit the scaling properties of the problem and vary the distance D between neighbour dipoles. It is then the relation between D and the Larmor radius R that becomes relevant.

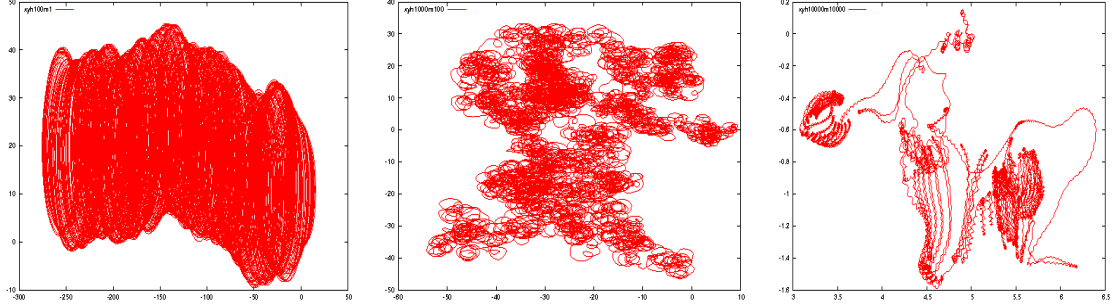


Figure 38. Trajectories in the (x,y) plane of a 10 GeV proton for $(H_0, M_0)=k(1000, 100)$ and $k=0.1, 1$ and 10 from left to right.

It is important at this stage to understand the scaling properties of the problem. Keeping $p_0=10$ GeV (in order to stay in the relativistic regime) we may multiply all fields by a factor k and divide all distances by the same factor while keeping the trajectories invariant. Indeed the transverse momentum kick over dx/k is the same as it would be with the original field over dx . However, for such an interpretation to be valid, one must also take into account the drift velocity of the shock front. Both the velocity of the particle and the velocity of the front are constants (the former is the light velocity and the latter is $\beta^*=0.75 \beta_{front}$ times the light velocity). As this scaling property is important to study what happens when the characteristic distance between perturbations is varied, it is worth taking the time to spell out its features in some detail. We may compare trajectories obtained for a field (H_0, M_0) with trajectories obtained for a field k times higher, $(H_0', M_0')=k(H_0, M_0)$. If, at the same time, we change the unit of distance, namely taking the distance between neighbour dipoles to be $D'=D/k$ instead of D , the calculated trajectories and the final energy distribution (namely the value of ρ) apply to both cases. For the particle to move by dl in the first case, it takes a time $dt=dl$ ($c=1$) during which the front progresses by $\delta=\beta^*dl$. In the second case, the particle has moved by $dl'=dl/k$ and the front by $\delta'=\beta^*dl/k$. Namely the same scaling law applies also to the movement of the front and we do not need to

change it when interpreting the trajectories with values of k that differ from unity. It must be clear that the fields are scaled, not the magnetic moments; when the dipoles are described by current loops, the field is multiplied by k and the radius of the loop is multiplied by $1/k$; the current is invariant and the magnetic moment is multiplied by $1/k^2$.

Figure 38 shows trajectories for $D=1$ and $(H_0, M_0)=(100,10)$, $(1000,100)$ and $(10000,1000)$. They may equally well be interpreted as trajectories for $(H_0, M_0)=(1000,100)$ and $D=0.1$, 1 and 10 . For $D=0.1$ (left panel) the Larmor radius is much larger than the distance between neighbour dipoles and the fluctuations are not sufficient to prevent the particle from drifting away. On the contrary, for $D=10$ (right panel) the distance between fluctuations is much larger than the Larmor radius and we are in the situation of a helical movement with characteristic magnetic mirror features. Such a high field may very well be able to trap the particle long enough in the front region to accelerate it significantly; the Larmor radius may then increase to a point where it matches the resonant distance between neighbour dipoles, resulting in an efficient acceleration. Such an extreme case is illustrated in Figure 39 where $D=1$ and $H_0 \sim M_0 \sim 25000$.

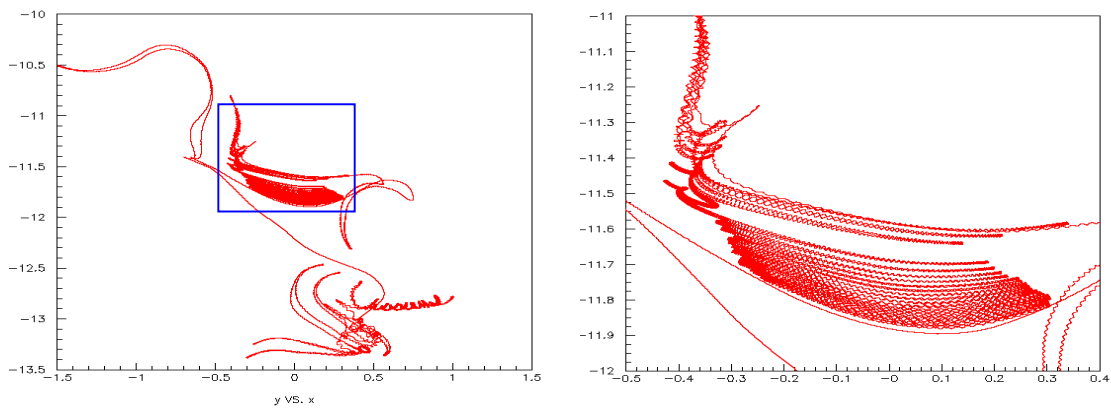


Figure 39. Trajectories in the (x,y) plane of a 10 GeV proton for $H_0 \sim M_0 \sim 25000$. The zoom of the blue rectangle displayed in the right panel illustrates the magnetic mirror effect.

4.5.4 Energy spectra

Energy spectra have been calculated for different values of H_0 and M_0 as a function of the distance D between neighbour dipoles, making use of the scaling properties described in the previous paragraph. Appendix 3 gives a summary of the simulations that have been made.

In practice, the simulation is made by keeping the distance between neighbour dipoles equal to 1 light second but multiplying H_0 and M_0 by $k=D$. To give an example a case $M_0=100 \mu\text{G}$, $H_0=50 \mu\text{G}$, $D=3 \text{ light seconds}$ is simulated as $M_0=300 \mu\text{G}$, $H_0=150 \mu\text{G}$, $D=1 \text{ light second}$. The acceleration efficiency is found to display a broad maximum above the region where both H_0 and M_0 exceed some 10 mG , corresponding to an average Larmor radius of typically a percent of the distance between neighbour dipoles. In such a regime, the magnetic mirror effect displayed in the right panel of *Figure 39* is very strong and the predictions of the simulation become significantly model dependent. What happens in practice is that the particle is trapped between two neighbour dipoles during a long period of time. If the particle is injected far away from the front it never reaches the front. If it is injected close enough to the front, as is done in the simulation, it may get trapped between two neighbour dipoles on either side of the front. It is clear that the idealization of the structure of perturbations made in the simulation becomes inadequate in such a case. In reality, ρ reaches its maximum (between 0.6 and 0.7) for Larmor radii of the order a percent of the distance between neighbour dipoles and higher fields, or equivalently smaller Larmor radii, are dominated by magnetic trapping and cannot be reliably modelled without having a precise knowledge of the real perturbations. *Figure 40* illustrates this well. It displays energy spectra obtained for the following values of the magnetic field: $H_0=M_0=10000$, 30000 and 100000 . In the case of the lower field value, with Larmor radii of the order of 10% of the distance between neighbour dipoles, the energy spectrum is still a power

law with index close to unity, as it is for lower field values whenever H_0 and M_0 are in the resonance region. But when the fields increase to 30 and 100 mG, namely when the Larmor radii reach the percent level and below, a bump appears at large accelerations, associated with particles being trapped between two dipoles on either side of the front.

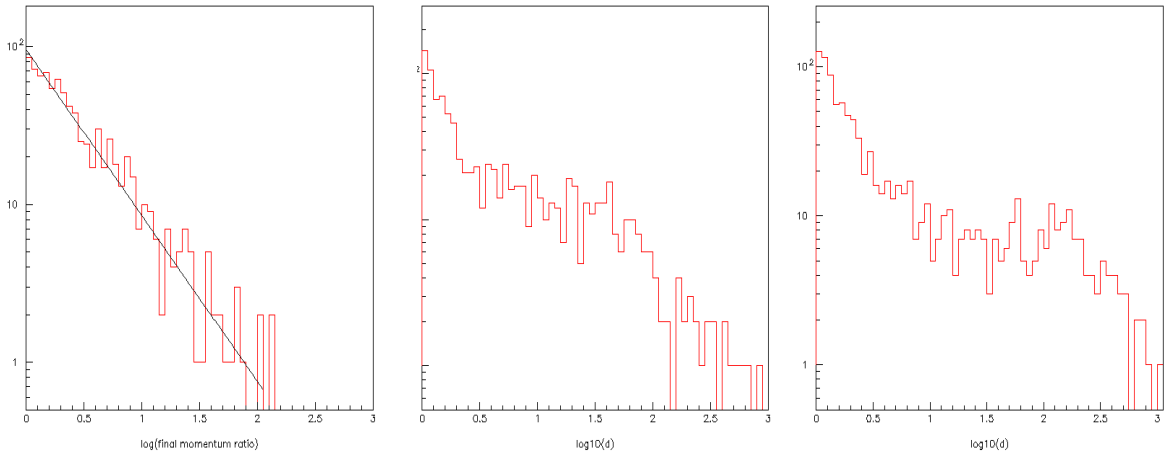


Figure 40. Distribution of $\log_{10}(E/E_0)$ in the H_0 - M_0 resonance region when moving toward smaller R/D values. $H_0=M_0=10000, 30000, 100000$ and $\rho=0.46, 0.61, 0.65$ from left to right respectively. The larger R/D case is fit to a power law with index \sim unity (black line). When R/D decreases a bump appears at large accelerations, associated with magnetic trapping between neighbour dipoles.

In summary, two conditions must be fulfilled for the acceleration to be efficient: H_0 and M_0 must obey a resonance relation and the Larmor radii must be small enough, say below a few percent, in comparison with the distance between neighbour dipoles. The resonance condition between H_0 and M_0 implies that the ratio between H_0 and M_0 be between $\sim 20\%$ at low fields and unity at high fields. When it is not satisfied, the energy spectra are cut-off because the particle escapes prematurely the shock region. This is illustrated in *Figure 41* where H_0 and M_0 are either in the resonance region (central panel) or outside (below in the left panel and above in the right panel).

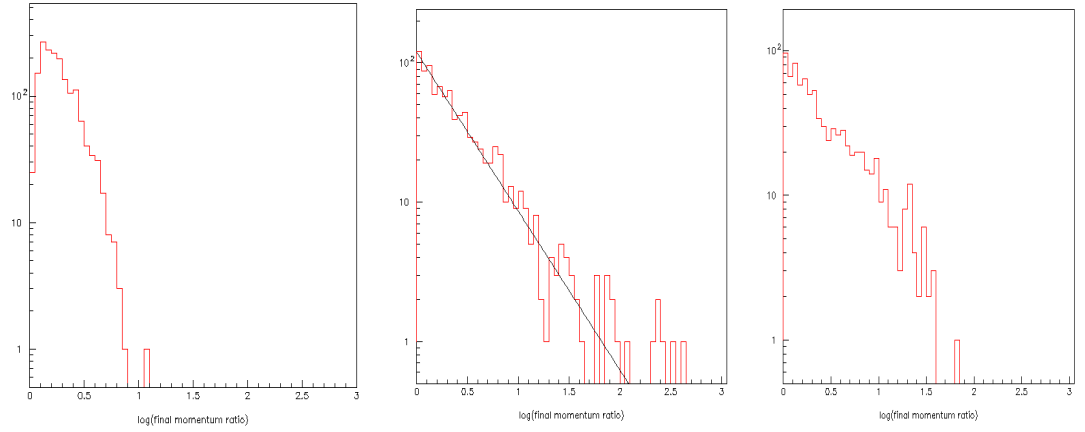


Figure 41. Distribution of $\log_{10}(E/E_0)$ below (left), on (center) and above (right) the H_0 - M_0 resonance region. From left to right, $H_0=1080, 3950, 0$, $M_0=27, 790, 1000$ and $\rho=0.27, 0.41, 0.42$ respectively. The resonance case (central panel) is fit to a power law with index \sim unity.

SUMMARY AND CONCLUSIONS

The simple simulation of the mechanism of diffusive shock acceleration presented here has illustrated several of its most important features. The main result has been to give evidence for the necessity of bouncing the particle being accelerated on magnetic turbulences rather than bending it a uniform magnetic field. A uniform magnetic field can only double the particle energy while magnetic turbulences, here modelled as a lattice of magnetic dipoles oriented at random but having a common magnetic moment, are able to increase the particle energy by several orders of magnitude.

For the acceleration to be efficient, the contribution of the turbulences to the total magnetic field must be commensurable with that of any uniform component that may subsist from the parent Supernova. Moreover the mesh size of the lattice, namely the characteristic scale separating neighbour turbulences, must be small enough with respect to the Larmor radius of the cosmic ray. Evidence for two such resonance-like relations is the main result of the present work. When acceleration proceeds, the Larmor radius increases, and the latter condition causes the cosmic ray to ultimately escape downstream. However, the condition is sufficiently loose to typically allow for acceleration by three orders of magnitudes.

Energy spectra are found to obey a power law with index close to unity when the conditions of acceleration are satisfied. When they are not, the main effect is the appearance of a cut-off associated with the premature escape of the cosmic ray downstream. The standard DSA calculation predicts a value of 2 for the index under the hypothesis of isotropy of the momenta and of an escape probability proportional to energy. The conditions realised in the present simulation are indeed more favourable.

It is important at this stage to underline the numerous approximations that have been made and the many differences that exist between model and reality. We list below the most relevant:

- The front is assumed to be planar but in reality it is rather spherical. Allowing for enough time, the particle that drifts downstream may ultimately meet again the shock inside which it is enclosed. In the case of a young Supernova, a few light years may be sufficient.
- The problem of injection has been ignored, the cosmic ray was assumed to have already reached an energy of 10 GeV before starting the acceleration cycle. In practice, such injection energy is indeed reasonable according to existing calculations.
- An essential feature that has been mentioned in several places is the interaction between the cosmic ray and the interstellar medium, producing streaming instabilities. This mechanism was completely ignored in the present work and a realistic simulation of the plasma waves induced by the accelerated cosmic rays is a very difficult problem. It was simply remarked that the energies involved in the magnetic turbulences are commensurate with that of the cosmic rays and that it was therefore very reasonable to assume that important interactions would result. It is also reasonable to assume that the scale that characterizes such turbulences is commensurate with the Larmor radius of the cosmic rays. But saying anything beyond these qualitative remarks is far from obvious and far beyond the scope of the present work.
- The choice of a cubic lattice of randomly oriented dipoles, all having the same magnetic moment, is certainly a sensible choice: it automatically satisfies Maxwell equations and gives a fair qualitative representation of turbulences. However, quantitatively, it is very far from reality and is a very crude picture of what is going on. In particular, in the case of small Larmor radii, it is too idealized to properly describe magnetic trapping: it reveals its possible importance, but cannot claim to achieve more than that.

- In reality, both the uniform magnetic field component and the magnetic turbulences have average amplitudes that depend on the distance to the shock front and, more importantly, are different upstream and downstream. This effect is ignored in the present model.
- Finally a compression ratio of 4, typical of hydrodynamic shocks, was assumed without justification.

It is clear from this list that the model used in the present simulation must limit its ambition to a qualitative illustration of the mechanism of diffusive shock acceleration. Its value is merely didactic. Yet, diffusive shock acceleration is such a complex process, difficult to visualize, that having a simple picture of it helps with a deeper understanding of its mechanism. In particular, the evidence obtained for the existence of resonances between the amplitudes of the dipole and uniform components on one hand, and between the distance between neighbour dipoles and the Larmor radius on the other are very general features that have been very well illustrated by the model.

More realistic models must be made in the framework of plasma physics. However, even the most sophisticated of these cannot hope for an accurate quantitative description of the real situation, the complexity of which is well beyond present modelling abilities.

APPENDIX 1: SHOCK DYNAMICS

In the shock frame:

The mass conservation gives:

$$\rho_1 v_1 = \rho_2 v_2$$

Momentum conservation gives:

$$\rho_1 v_1^2 + p_1 = \rho_2 v_2^2 + p_2$$

And energy conservation gives:

Where $\gamma = \frac{C_p}{C_v} = \frac{(3+2n)}{(1+2n)}$ (n atoms/molecule), $v_s = \sqrt{\frac{\gamma p}{\rho}}$ is the sound velocity and

$M = \frac{v}{v_s}$ is the Mach number.

From three equations, we have:

$$\frac{p_2}{\rho_2} = -v_2^2 + \frac{p_1}{\rho_2} + \frac{\rho_1 v_1^2}{\rho_2} = -v_2^2 + \frac{p_1}{\rho_2} + v_1 v_2$$

$$\frac{(v_1 - v_2)(v_1 + v_2)}{2} = \frac{\gamma}{\gamma - 1} \left(\frac{p_2}{\rho_2} - \frac{p_1}{\rho_1} \right) = \frac{\gamma}{\gamma - 1} \left(-v_2^2 + \frac{p_1}{\rho_2} + v_1 v_2 - \frac{p_1}{\rho_1} \right)$$

$$\frac{(v_1 - v_2)(v_1 + v_2)}{2} = \frac{\gamma}{\gamma - 1} \left[v_2(v_1 - v_2) + \frac{p_1}{\rho_2} - \frac{p_1}{\rho_1} \right]$$

$$\frac{(v_1 - v_2)(v_1 + v_2)}{2} = \frac{\gamma}{\gamma - 1} \left[v_2(v_1 - v_2) + \frac{p_1}{\rho_1} \left(\frac{\rho_1}{\rho_2} - 1 \right) \right]$$

$$\frac{(v_1 - v_2)(v_1 + v_2)}{2} = \frac{\gamma}{\gamma - 1} \left[v_2(v_1 - v_2) + \frac{p_1}{\rho_1} \frac{v_2 - v_1}{v_1} \right]$$

$$\frac{(v_1 + v_2)}{2} = \frac{\gamma}{\gamma - 1} \left[v_2 - \frac{p_1}{\rho_1 v_1} \right]$$

$$\frac{(v_1 + v_2)}{2} = \frac{\gamma}{\gamma - 1} v_2 - \frac{1}{\gamma - 1} \frac{\gamma p_1}{\rho_1} \frac{1}{v_1}$$

$$\frac{\gamma p_1}{\rho_1} = \frac{v_1^2}{M_1^2}$$

Then we have

$$\frac{(v_1 + v_2)}{2} = \frac{\gamma}{\gamma - 1} v_2 - \frac{1}{\gamma - 1} \frac{v_1^2}{M_1^2} \frac{1}{v_1} = \frac{\gamma}{\gamma - 1} v_2 - \frac{1}{\gamma - 1} \frac{v_1}{M_1^2}$$

$$\frac{v_1}{v_2} = \frac{\gamma+1}{\gamma-1+2M_1^{-2}}$$

For large M and monoatomic gases.

The compression ratio is $r = \frac{\rho_2}{\rho_1} = \frac{v_1}{v_2} = \frac{\gamma+1}{\gamma-1} = 4$ for monoatomic gases ($\gamma=5/3$) and for

large M.

In such a way we have:

$$\frac{p_2}{\rho_2} = \frac{v_1^2 - v_2^2}{2} \frac{(\gamma-1)}{\gamma} + \frac{p_1}{\rho_1}$$

$$\frac{p_2}{p_1} \frac{\rho_1}{\rho_2} = \frac{v_1^2 - v_2^2}{2} \frac{(\gamma-1)\rho_1}{\gamma p_1} + 1$$

$$\frac{p_2}{p_1} \frac{v_2}{v_1} = \frac{\gamma-1}{2} \frac{v_1^2 \rho_1}{\rho_1} \left[1 - \frac{v_2^2}{v_1^2}\right] + 1 = \frac{\gamma-1}{2} M_1^2 \left[1 - \left(\frac{v_2}{v_1}\right)^2\right] + 1$$

$$\frac{p_2}{p_1} \frac{v_2}{v_1} = \frac{\gamma-1}{2} M_1^2 \left[1 - \left(\frac{\gamma-1+2M_1^{-2}}{\gamma+1}\right)^2\right] + 1$$

$$\frac{p_2}{p_1} \frac{v_2}{v_1} = \frac{\gamma-1}{2} M_1^2 \frac{(\gamma+1)^2 - (\gamma-1+2M_1^{-2})^2}{(\gamma+1)^2} + 1 = \frac{\gamma-1}{2} M_1^2 \frac{4(1-M_1^{-2})(\gamma+M_1^{-2})}{(\gamma+1)^2} + 1$$

$$\frac{p_2}{p_1} \frac{v_2}{v_1} = \frac{2(\gamma-1)(\gamma M_1^2 + 1 - \gamma - M_1^{-2}) + (\gamma+1)^2}{(\gamma+1)^2}$$

$$\frac{p_2}{p_1} \frac{v_2}{v_1} = \frac{2(\gamma-1)\gamma M_1^2 - (\gamma-1)^2 - 2(\gamma-1)M_1^{-2} + (\gamma+1)^2 - (\gamma-1)^2}{(\gamma+1)^2}$$

$$\frac{p_2}{p_1} \frac{v_2}{v_1} = \frac{2(\gamma-1)\gamma M_1^2 - (\gamma-1)(\gamma-1+2M_1^{-2}) + 4\gamma}{(\gamma+1)^2}$$

$$\frac{p_2}{p_1} \frac{v_2}{v_1} = \left[\frac{2\gamma}{M_1^{-2}} (\gamma-1+2M_1^{-2}) - (\gamma-1)(\gamma-1+2M_1^{-2}) \right] \frac{1}{(\gamma+1)^2}$$

$$\frac{p_2}{p_1} \frac{v_2}{v_1} = \frac{\gamma-1+2M_1^{-2}}{\gamma+1} \left[\frac{2\gamma}{M_1^{-2}} - (\gamma-1) \right] \frac{1}{(\gamma+1)}$$

$$\frac{p_2}{p_1} \frac{v_2}{v_1} = \frac{v_2}{v_1} \frac{2\gamma M_1^2 - (\gamma-1)}{\gamma+1}$$

$$\frac{p_2}{p_1} = \frac{2\gamma M_1^2 - (\gamma-1)}{\gamma+1}$$

Use the equation for ideal gases:

$$\frac{P_1 V_1}{T_1} = \frac{P_2 V_2}{T_2} \Rightarrow \frac{T_2}{T_1} = \frac{P_2 V_2}{P_1 V_1} = \frac{P_2}{P_1} \frac{\rho_1}{\rho_2} = \frac{P_2}{P_1} \frac{v_2}{v_1}$$

$$\frac{T_2}{T_1} = \frac{2\gamma M_1^2 - (\gamma - 1)}{\gamma + 1} \frac{\gamma - 1 + 2M_1^{-2}}{\gamma + 1}$$

As for monatomic ideal gases ($\gamma=5/3$) and large Mach number, we have

$$\frac{T_2}{T_1} = \frac{5M_1^2 - 1}{4} \frac{1 + 3M_1^{-2}}{4}$$

$$\frac{T_2}{T_1} = \frac{5M_1^2 + 14 - 3M_1^{-2}}{16}$$

However, once in region 2, particle may escape the shock region with a probability P_{esc} .

$$P_{\text{esc}} = \frac{\Phi_{\text{esc}}}{\Phi_{\text{ud}}}, \quad \Phi_{\text{ud}} = \frac{1}{4 \cdot \mathbf{n}_0 \cdot \mathbf{v}}, \quad \Phi_{\text{esc}} = n_0 v_2$$

$$\text{Then } P_{\text{esc}} = \frac{4v_2}{v} = \left(\frac{4}{r}\right) \cdot \left(\frac{v_{\text{shock}}}{v}\right) = \left(\frac{4}{r}\right) \cdot \beta_{\text{shock}}$$

In this region, the scattering centres move away from the shock at velocity $v_2 \sim 1/4 v_{\text{shock}}$ while the particle moves at light velocity at varying angles to the shock

APPENDIX 2: SIMULATION CODE

```

program dsa
  common/hxyz/hx0,hy0,hz0,xmag(100,50,50),ymag(100,50,50),
&      zmag(100,50,50)
  save
  double precision t0,dt0,step
  real*4 xstep,x0
  data step1,step2/0.,150000./
  data px00/10./
c
c   the add 19/04/2010
  integer*4 timeArray(3)
c
c   real*8 t0,x0,y0,z0
c
c   diffusive shock acceleration
c
c   young supernovae expand at 1% of light velocity for some 10**4 years,
meaning a radius of some 100 lyr,
c
c   some 10 or so percent of the final radius before dissolution in ISM
c
c   a field of 1 microgauss =1E-10 T over 1 light second=3E8 m
c
c   gives a transverse momentum kick of 3E-2 Tm *0.3GeV= 9E-3 GeV.
c
c   Take as units GeV, lightseconds and microgauss. Take c=1.
c
c   1 unit of field over 1 unit of distance means a transverse kick of
0.009 GeV.
c
c   kick=0.009*Bdl For dl=step, take kick=0.1p Then step=0.1p/(0.009B),
say=10p/B
c
c   p is followed from 0.1 GeV to 1 TeV typically, i.e. Larmor radius
varies from 0.33/H to 3300/H
c
c   Taking H =10 microGauss, this means from .033 to 330 light seconds
c
c   Use cells of one light second and field irregularities of then same
size
c
c   Take x>0 upstream (undisturbed ISM) and <0 downstream (cotaining SNR)
c
c   Upstream the shock approaches at velocity vfront=0.01, downstream it
moves away at velocity vfront/4=0.0025 (monoatomic gas)
c
c   But in both cases the other medium approaches at velocity
beta=3vfront/4=0.0075
c
c   x=0 remains on the shock
c
c
c
c   *****
c
c   tracking
c
c
c
c   define ntrav the number of front crossings
  call hlimap(20000,'ONW')
  call hbook1(20,' log(final momentum ratio)', 60.,0.,3.,0.)
  call hbook1(21,'log(total time)',100.,3.,13.,0.)
  call init
c
c   The add 19/04/10
c
c   call itime(timeArray)
c
c   i=rand(timeArray(1)+timeArray(2)+timeArray(3))
c
c   print*,timeArray(1),timeArray(2),timeArray(3)
c
c   do 1 k=1,50
c
c   print*,'time!!!!!!!!!!!!!!!!!!!!!!',rand(0)
c
c   1 continue
c
c   The end

```

```

loop=0
999 continue
loop=loop+1
tacc=0.
ntrav=0
vfront=.02
x0=20.+40.*rand()
y0=-20.+40.*rand()
z0=-20.+40.*rand()

pz0=0.
t0=0.
px0=px00
py0=0.
p02=px0**2+py0**2+pz0**2
p0=sqrt(p02)
e0=sqrt(1.+p02)
xstep=0.
kescape=0
eold=0.
beta=3.*vfront/4.
gamma=1./sqrt(1.-beta**2)
gabeta=gamma*beta
100 continue

xstep=xstep+1.

if(xstep.eq.16770000.) xstep=0.
call field(x0,y0,z0,hx,hy,hz)
hh=sqrt(hx**2+hy**2+hz**2)
step=3.3*p0/hh
if(step.gt.0.1) step=0.1
px0=px0+0.009*(hy*pz0-hz*py0)/p0*step
py0=py0+0.009*(hz*px0-hx*pz0)/p0*step
pz0=pz0+0.009*(hx*py0-hy*px0)/p0*step
pp0=sqrt(px0**2+py0**2+pz0**2)
px0=px0*p0/pp0
py0=py0*p0/pp0
pz0=pz0*p0/pp0
x1=x0+step*px0/p0
y0=y0+step*py0/p0
z0=z0+step*pz0/p0
ystep=float(ifix(xstep/100000.))*100000.
if(xstep.eq.ystep)then
c   print*,'runing',loop,xstep,x0,y0,z0,e0,t0,step,hh
   anew=e0
   if(enew.le.eold.and.x0.lt.-3000.)then
     kescape=kescape+1
   endif
   if(enew.gt.eold.or.x0.gt.-3000.)then
     kescape=0
     eold=enew
   endif
endif

```

```

        if(kescape.ge.5.and.x0.lt.-3000.) then
            call hf1(20,alog10(pp0/px0),1.)
            call hf1(21,alog10(tacc),1.)
c           write(11,*) loop,tacc,pp0,px0,py0,pz0
c           print*,'new !!!',loop,x0,e0,t0,tacc
            go to 999
        endif
    endif
    dt0=e0*step/p0
    t0=t0+dt0
    if(x0.gt.0.) x1=x1-vfront*dt0
    if(x0.lt.0.) x1=x1-0.25*vfront*dt0
    if(x1*x0.ge.0.)then
        x0=x1
        goto 100
    endif
    if(x1*x0.lt.0.)then
        ntrav=ntrav+1
        tacc=t0
        sign=1.
        if(x0.gt.0.)sign=-1.
        e1=gamma*e0+sign*gabeta*px0
        px1=gamma*px0+sign*gabeta*e0
        x0=x1
        e0=e1
        px0=px1
        p0=sqrt(e0**2-1.)
    endif
    go to 100
    stop
end
c
subroutine init
common/hxyz/hx0,hy0,hz0,xmag(100,50,50),ymag(100,50,50),
&      zmag(100,50,50)
save
data teta0,phi0,h0,dipole
&      /0.,0.,249.,12.5/
teta0=teta0*3.14159/180.
cteta0=cos(teta0)
steta0=sin(teta0)
phi0=phi0*3.14159/180.
cphi0=cos(phi0)
sphi0=sin(phi0)
hz0=h0*cteta0
hx0=h0*steta0*cphi0
hy0=h0*steta0*sphi0
do i=1,100
    do j=1,50
        do k=1,50
            cteta=-1.+2.*rand()
            steta=sqrt(1.-cteta**2)
            phi=2.*3.14159*rand()

```

```

        xmag(i,j,k)=dipole*steta*sin(phi)
        ymag(i,j,k)=dipole*steta*cos(phi)
        zmag(i,j,k)=dipole*cteta
    enddo
enddo
return
end
subroutine field(x0,y0,z0,hx,hy,hz)
external jcell
common/hxyz/hx0,hy0,hz0,xmag(100,50,50),ymag(100,50,50),
&      zmag(100,50,50)
save
double precision t0,dt0,step
dimension x(3),y(3),z(3),jx(3),jy(3),jz(3)
x(2)=float(ifix(abs(x0)))+.5
if(x0.lt.0) x(2)=-x(2)
x(1)=x(2)-1.
x(3)=x(2)+1.
y(2)=float(ifix(abs(y0)))+.5
if(y0.lt.0) y(2)=-y(2)
y(1)=y(2)-1.
y(3)=y(2)+1.
z(2)=float(ifix(abs(z0)))+.5
if(z0.lt.0) z(2)=-z(2)
z(1)=z(2)-1.
z(3)=z(2)+1.
do i=1,3
    jx(i)=jcell(x(i),1)
    jy(i)=jcell(y(i),2)
    jz(i)=jcell(z(i),3)
enddo
c
hx=hx0
hy=hy0
hz=hz0
do i=1,3
    rx=-x(i)+x0
    jxi=jx(i)
    do j=1,3
        ry=-y(j)+y0
        jyj=jy(j)
        do k=1,3
            rz=-z(k)+z0
            jzk=jz(k)
            r2=rx**2+ry**2+rz**2
            r=sqrt(r2)
            r3=r2**1.5
            r5=r3*r2
            xmagijk=xmag(jxi,jyj,jzk)
            ymagijk=ymag(jxi,jyj,jzk)
            zmagijk=zmag(jxi,jyj,jzk)
            rm=rx*xmagijk+ry*ymagijk+rz*zmagijk

```

```

        if(r.ge.0.5)then
            hx=hx+3.*rm*rx/r5-xmagijk/r3
            hy=hy+3.*rm*ry/r5-ymagijk/r3
            hz=hz+3.*rm*rz/r5-zmagijk/r3
        endif
        if(r.eq.0.)then
            hx=hx+16.*xmagijk
            hy=hy+16.*ymagijk
            hz=hz+16.*zmagijk
        endif
        if(r.gt.0..and.r.lt.0.5)then
            hx=hx+16.*(r*(3.*rm*rx/r2-xmagijk)+(1.-2.*r)*xmagijk)
            hy=hy+16.*(r*(3.*rm*ry/r2-ymagijk)+(1.-2.*r)*ymagijk)
            hz=hz+16.*(r*(3.*rm*rz/r2-zmagijk)+(1.-2.*r)*zmagijk)
        endif
    enddo
enddo
return
end
c
integer function jcell(u,i)
du =25.
if(i.eq.1) du=50.
u1=u
if(u1.lt.-du) then
    uu=- (u1+du)/2./du
    uu=u1+2.*du*(1.+float(ifix(uu)))+du
endif
if(u1.ge.du) then
    uu=(u1+du)/2./du
    uu=u1+du-2.*du*float(ifix(uu))
endif
if(u1.ge.-du.and.u1.lt.du) uu=u1+du
jcell=ifix(uu)+1
return
end

```

APPENDIX 3: SIMULATION RUNS

The table below lists the parameters used in the simulation data.

H_0 is the value of the uniform field in μG as given in the program.

M_0 is the value of the dipole field in μG as given in the program.

f is a factor by which the time has been scaled in some cases.

ρ is the mean value of $\log_{10}(E/E_0)$ after acceleration.

Rms is the root mean square value of $\log_{10}(E/E_0)$ after acceleration.

N is the number of trajectories that have been generated.

Nr	H0	M0	L	ρ	Rms	N
1	0	2	1	0.054	0.045	2110
2	0	10	1	0.145	0.103	1846
3	0	25	1	0.120	0.103	2171
4	0	50	1	0.261	0.183	3428
5	0	75	1	0.254	0.187	2372
6	0	100	1	0.339	0.236	1800
7	0	150	1	0.369	0.281	1772
8	0	200	1	0.385	0.309	2677
9	0	300	1	0.404	0.337	2106
10	0	400	1	0.394	0.330	1414
11	0	1000	1	0.420	0.368	842
12	0	3000	1	0.462	0.421	138
13	0	10000	1	0.520	0.510	469
14	0	50000	1	0.886	0.780	245
15	0	100000	1	0.937	0.855	272
16	0	200000	1	0.837	0.873	254
17	0	600000	1	0.622	0.897	208
18	0	2316000	1	0.135	0.291	222
19	25	5	1	0.349	0.304	5417
20	25	10	1	0.391	0.361	1521
21	25	15	1	0.398	0.380	3866
22	25	20	1	0.348	0.346	4982
23	25	25	1	0.309	0.306	1987
24	25	50	1	0.239	0.211	1897
25	25	75	1	0.279	0.207	1362
26	25	100	1	0.295	0.221	1459
27	50	5	1	0.319	0.251	2146

28	50	10	1	0.331	0.283	2333
29	50	15	1	0.358	0.321	2534
30	50	20	1	0.387	0.359	3367
31	50	30	1	0.380	0.356	7283
32	50	40	1	0.347	0.341	2951
33	50	45	1	0.340	0.332	2749
34	50	50	1	0.330	0.318	2636
35	50	55	1	0.314	0.291	1292
36	50	65	1	0.315	0.281	3918
37	50	75	1	0.306	0.263	2713
38	50	80	1	0.308	0.258	3623
39	50	90	1	0.316	0.256	2986
40	50	90	1	0.357	0.297	855
41	50	100	1	0.320	0.256	2097
42	50	120	1	0.339	0.262	1417
43	50	150	1	0.346	0.264	1460
44	50	200	1	0.372	0.286	8782
45	75	5	1	0.289	0.194	16420
46	75	10	1	0.320	0.259	3992
47	75	15	1	0.349	0.298	3219
48	75	20	1	0.367	0.336	3605
49	75	25	1	0.392	0.359	2783
50	75	50	1	0.386	0.368	4646
51	75	75	1	0.338	0.325	937
52	100	5	1	0.267	0.144	2074
53	100	10	1	0.304	0.235	13757
54	100	15	1	0.341	0.285	1550
55	100	20	1	0.348	0.299	1304
56	100	25	1	0.372	0.339	1102
57	100	50	1	0.385	0.368	2479
58	100	75	1	0.382	0.363	1812
59	100	100	1	0.364	0.322	1543
60	100	200	1	0.379	0.300	1405
61	100	400	1	0.394	0.339	4377
62	200	5	1	0.244	0.092	3926
63	200	10	1	0.266	0.160	3827
64	200	15	1	0.302	0.224	3019
65	200	20	1	0.325	0.256	2781
66	200	25	1	0.340	0.291	2504
67	200	50	1	0.388	0.358	1592

68	200	75	1	0.431	0.394	1740
69	200	100	1	0.429	0.392	1282
70	200	150	1	0.418	0.409	658
71	200	200	1	0.419	0.373	1703
72	200	400	1	0.397	0.342	6065
73	250	40	1	0.365	0.342	4211
74	250	50	1	0.385	0.395	2415
75	250	100	1	0.426	0.312	1786
76	0	2	1	0.050	0.050	12884
77	0.5	2	1	0.187	0.168	1965
78	1	2	1	0.327	0.278	2141
79	2	2	1	0.410	0.360	2276
80	4	2	1	0.399	0.363	1935
81	7	2	1	0.374	0.348	897
82	10	2	1	0.345	0.297	1706
83	30	2	1	0.314	0.213	1155
84	40	2	1	0.300	0.147	2028
85	0	10	1	0.153	0.110	1484
86	1	10	1	0.190	0.148	2803
87	2	10	1	0.326	0.266	954
88	3	10	1	0.318	0.265	2775
89	5	10	1	0.420	0.372	2527
90	7	10	1	0.413	0.387	2277
91	10	10	1	0.412	0.392	1719
92	30	10	1	0.384	0.354	1433
93	40	10	1	0.351	0.328	1502
94	1000	0	1	0.301	0.301	798
95	860	51	1	0.319	0.245	1213
96	710	71	1	0.355	0.311	1167
97	510	86	1	0.418	0.361	1136
98	400	92	1	0.406	0.368	900
99	200	100	1	0.394	0.361	900
100	100	100	1	0.364	0.322	1543
101	0	100	1	0.283	0.205	898
102	100	0	1	0.245	0.013	549
103	86	5	1	0.234	0.114	900
104	71	7	1	0.254	0.162	900
105	51	9	1	0.282	0.212	900
106	40	9	1	0.308	0.233	489
107	20	10	1	0.367	0.313	632

108	10	10	1	0.384	0.324	533
109	0	10	1	0.153	0.110	1484
110	270	6.78	1	0.220	0.060	5446
111	539	13.54	1	0.247	0.188	3054
112	1077	27.02	1	0.265	0.158	1648
113	2148	53.91	1	0.292	0.213	3081
114	4285	107.55	1	0.340	0.260	847
115	8548	214.55	1	0.335	0.283	624
116	249	12.48	1	0.250	0.170	1561
116	497	24.91	1	0.294	0.204	1472
117	992	49.72	1	0.327	0.251	1463
118	1980	99.18	1	0.357	0.293	3333
119	3950	197.87	1	0.379	0.324	1439
120	7879	394.75	1	0.406	0.324	2061
122	197	20	1	0.320	0.270	10199
123	393	39	1	0.344	0.290	1224
124	785	78	1	0.383	0.330	2054
125	1566	157	1	0.410	0.370	1296
126	3124	312	1	0.410	0.390	794
127	6232	623	1	0.440	0.420	788
129	125	25	1	0.359	0.335	1724
130	249	50	1	0.394	0.353	2595
131	497	99	1	0.405	0.374	1356
132	992	198	1	0.424	0.387	1554
133	1979	395	1	0.429	0.405	3718
134	3949	788	1	0.404	0.401	945
136	68	27	1	0.391	0.382	1724
137	135	54	1	0.418	0.386	1692
138	270	108	1	0.426	0.408	2272
139	539	215	1	0.428	0.411	1409
140	1076	428	1	0.428	0.405	1480
141	2147	855	1	0.420	0.380	3718
143	4	3	1	0.254	0.208	1168
144	8	6	1	0.290	0.245	1198
146	16	13	1	0.316	0.283	8418
147	35	28	1	0.413	0.406	2381
148	69	55	1	0.406	0.388	1833
149	139	110	1	0.396	0.375	2238
150	277	220	1	0.405	0.380	2050
151	552	438	1	0.404	0.367	6215

152	1101	874	1	0.455	0.388	857
153	1355	1076	1	0.403	0.366	235
154	2912	2312	1	0.438	0.382	394
155	6262	4972	1	0.487	0.473	424
156	13462	10689	1	0.650	0.570	172
157	28944	22981	1	0.690	0.780	449
158	62229	49410	1	0.800	0.800	347
159	1078	27	1	0.265	0.156	1648
160	994	50	1	0.327	0.251	1463
161	785	80	1	0.383	0.330	2054
162	498	100	1	0.405	0.374	1356
163	271	108	1	0.426	0.408	1409
164	139	111	1	0.396	0.375	2238
165	110	110	1	0.364	0.322	1534
166	92	111	1	0.368	0.315	810
167	74	111	1	0.345	0.272	450
168	50	100	1	0.320	0.256	2097
169	37	111	1	0.327	0.247	1317
170	28	111	1	0.324	0.242	1313
171	4285	107	1	0.322	0.250	1508
172	3955	197	1	0.379	0.324	1439
173	3127	312	1	0.410	0.390	4794
174	1981	394	1	0.429	0.393	825
175	1077	428	1	0.428	0.405	3718
176	553	438	1	41.000	0.370	6215
177	444	444	1	0.386	0.340	769
178	296	444	1	0.402	0.342	921
179	143	444	1	0.380	0.330	998
180	8548	215	1	0.335	0.283	624
181	7879	275	1	0.406	0.324	2061
182	6232	623	1	0.442	0.421	788
183	3949	788	1	0.404	0.401	945
184	2147	854	1	0.420	0.380	457
185	1101	874	1	0.397	0.361	745
186	732	890	1	0.410	0.370	962
187	570	853	1	0.380	0.340	442
188	428	856	1	0.355	0.308	143
189	214	856	1	0.374	0.327	221
190	1110	0	1	0.301	0.000	800
191	961	56	1	0.340	0.266	800

192	785	80	1	0.385	0.336	799
193	555	96	1	0.397	0.364	635
194	461	101	1	0.396	0.350	707
195	232	109	1	0.426	0.393	730
196	111	111	1	0.390	0.342	775
197	92	111	1	0.368	0.315	810
198	74	111	1	0.335	0.287	511
199	55	111	1	0.322	0.266	511
200	37	111	1	0.327	0.247	1317
201	28	111	1	0.324	0.242	1313
202	11	111	1	0.304	0.229	874
203	1	111	1	0.322	0.242	805
204	0	111	1	0.240	0.196	699
205	10000	1000	100	0.001	0.004	900
206	3000	300	30	0.007	0.006	900
207	1000	100	10	0.028	0.022	900
208	300	30	3	0.101	0.076	900
209	100	10	1	0.270	0.180	900
213	30	3	0.3	1.270	0.915	295
214	10	1	0.1	2.632	0.927	500
215	5	0.5	0.05	1.770	0.140	307
216	1	0.1	0.01	0.733	0.398	148
217	0.3	0.03	0.003	0.365	0.061	218
218	0.1	0.01	0.001	0.142	0.011	148
219	30000	3000	30	0.011	0.023	400
220	10000	1000	10	0.042	0.049	983
221	3000	300	3	0.138	0.133	804
222	1000	100	1	0.368	0.323	718
223	300	30	0.3	1.308	1.050	212
224	100	10	0.1	2.380	0.911	139
225	50	5	0.05	2.859	0.120	137
226	10	1	0.01	1.850	0.225	285
227	3	0.3	0.003	1.200	0.100	334
228	1	0.1	0.001	0.692	0.035	152
229	6	3	0.03	0.452	0.742	73
230	20	10	0.1	1.930	0.810	224
231	60	30	0.3	1.021	0.755	400
232	200	100	1	0.394	0.361	900
233	600	300	3	0.430	0.523	600
234	2000	1000	10	0.057	0.080	500
235	6000	3000	30	0.014	0.035	500
237	0	1.11	0.01	0.008	0.08	690

238	0	11.1	0.1	0.082	0.072	723
239	0	24.3	0.219	0.163	0.126	700
240	0	52	0.468	0.244	0.153	510
241	0	100	1	0.24	0.236	1800
242	0	240	2.13	0.198	0.187	900
243	0	507	4.57	0.09	0.08	523
244	0	1110	10	0.072	0.103	567
245	0	2373	21.4	0.034	0.097	900
246	0	11100	100	0.001	0.003	815
247	8	0.8	0.01	0.034	0.285	303
248	79	7.85	0.1	2.681	0.92	512
249	236	23.6	0.3	1.244	1.063	181
250	785	78.5	1	0.385	0.336	799
251	2355	236	3	0.128	0.125	1297
252	7850	785	10	0.04	0.041	1335
253	10	1	0.1	2.63	0.93	500
254	10	1	0.3	1.1	0.416	700
255	10	1	0.5	0.499	0.227	400
256	10	1	1	0.192	0.07	569
1	100000	100000	1	0.65	0.75	985
2	100000	30000	1	0.582	0.642	1044
3	30000	10000	1	0.47	0.49	1000
4	30000	30000	1	0.61	0.634	1000
5	30000	100000	1	0.64	0.76	1000
6	30000	300000	1	0.56	0.76	1000
7	10000	10000	1	0.462	0.474	900
8	10000	30000	1	0.592	0.64	1410
9	10000	100000	1	0.666	0.756	451
10	10000	300000	1	0.57	0.75	1200
11	3000	10000	1	0.48	0.48	887
12	3000	30000	1	0.58	0.63	1410
13	3000	100000	1	0.65	0.76	1000
14	3000	300000	1	0.57	0.75	1417
15	1000	30000	1	0.604	0.66	1000
16	1000	100000	1	0.617	0.718	1000

REFERENCES

1. J. Abraham et al. (Auger Collaboration), *Correlation of the highest energy cosmic rays with nearby extra-galactic objects*, Science 318 (2007) 938].
2. J.A. Hinton (HESS Collaboration), New Astronomy Review 48 (2004) 331.
3. H. Muraishi et al. (CANGAROO Collaboration), Astron. And Astrophys. 354 (2000) L57 ;
R. Enomoto et al. (CANGAROO Collaboration), Nature 416 (2002) 823.
4. F. Aharonian et al. (HESS Collaboration) Nature 432 (2004) 75.
5. E. Pfefermann and B. Aschenbach, *ROSAT observation of a new SNR in constellation Scorpius*, Röntgenstrahlung from the Universe, 1996, 267.
6. D.C. Ellison, A. Decourchelle and J. Ballet, Astr. & Astrophys. 413 (2004) 189.
7. Y. Uchiyama et al., Nature 449 (2007) 576 and references therein.
8. R. Blandford and D. Eichler, Phys. Rep. 154 (1987) 1;
S.P. Reynolds, Astrophys. J. 493 (1998) 375;
Y. Jiang et al., arXiv : 0904.4918 (2009);
E.G. Berezhko and D.C. Ellison, Astrophys. J. 526 (1999) 385;
E.G. Berezhko and H.J. Völk, Astron. and Astrophys. 451 (2006) 981;
D.C. Ellison et al., Astrophys. J. 661 (2007) 879;
A.E. Vladimirov, Astrophys. J. 688 (2008) 1084.
9. Most of this chapter and of the two chapters following makes use of information available in the lecture notes of P. Darriulat.
10. <http://prop.hfradio.org>.
11. <http://www.nasa.gov/topics/solarsystem/sunearthsystem/main/News080210-cme.html>
12. J. Abraham et al. (Pierre Auger Collaboration), Science 318 (2007) 938;
F. Schmidt et al. (Pierre Auger Collaboration), Astropart. Phys. 29 (2008) 355.